ELSEVIER

Sinuous ridges in Chukhung crater, Tempe Terra, Mars: Implications for fluvial, glacial, and glaciofluvial activity

Frances E.G. Butcher [a],[*],[1], Matthew R. Balme [a], Susan J. Conway [b], Colman Gallagher [c],[d], Neil S. Arnold [e], Robert D. Storrar [f], Stephen R. Lewis [a], Axel Hagermann [g], Joel M. Davis [h]

[a] School of Physical Sciences, The Open University, Walton Hall, Milton Keynes MK7 6AA, UK
[b] CNRS, UMR 6112 Laboratoire de Planétologie et Géodynamique, Université de Nantes, France
[c] UCD School of Geography, University College Dublin, Dublin 4, Ireland
[d] UCD Earth Institute, University College Dublin, Dublin 4, Ireland
[e] Scott Polar Research Institute, University of Cambridge, Cambridge CB2 1ER, UK
[f] Department of the Natural and Built Environment, Sheffield Hallam University, Sheffield, S1 1WB, UK
[g] Biological and Environmental Sciences, University of Stirling, Stirling FK9 4LA, UK
[h] Department of Earth Sciences, Natural History Museum, London, UK

ARTICLE INFO

ABSTRACT

We present a geomorphic map of Chukhung crater (38.47°N, 72.42°W) in central Tempe Terra, Mars. Chukhung crater formed ~3.6–2.1 Ga, between the early Hesperian and early Amazonian periods of Mars' geologic history. It hosts dendritic networks of crater wall valleys, broad crater floor valleys, mid- to late-Amazonian-aged debris-covered glaciers, moraine-like deposits, and a radial assemblage of sinuous ridge landforms. We explore the origins of landforms in Chukhung crater, focusing in particular upon the sinuous ridges. In northern Chukhung crater, sinuous ridges extend downslope from fluvial valley systems on the northern crater wall. We interpret the northern sinuous ridges as inverted paleochannels: ridges formed by exhumation of resistant and/or indurated fluvial channel fill deposits. The origins of sinuous ridges on the southern floor of Chukhung crater are more ambiguous. They emerge from beneath moraine-like ridges which bound extant debris-covered glaciers extending from the southern wall of the crater. The southern sinuous ridges have numerous morphological and contextual similarities to eskers: ridges of glaciofluvial sediment deposited in meltwater conduits within or beneath wet-based glaciers. The close proximity of the northern and southern sinuous ridges, however, calls into question an interpretation which ascribes a different origin to each set. The similarity in the overarching process between esker and inverted channel formation (i.e., exposure by the removal of a bounding medium, be that ice or sediments/rock) results in convergence of form between eskers and inverted paleochannels. We discuss the esker-like characteristics of the southern sinuous ridges in detail, and argue that one of two ridge populations in southern Chukhung crater is best explained by the esker hypothesis while the other could be explained under either the esker or the inverted paleochannel hypothesis. Regardless of the specific formation mechanism for the southern sinuous ridges, we find that Chukhung crater has undergone significant modification by liquid water since its formation. The northern sinuous ridges and associated crater-wall valleys provide evidence for subaerial drainage of precipitation and/or snowmelt. This suggests that Chukhung crater, and possibly the surrounding region, experienced unusually warm and wet episodes between the early Hesperian and mid Amazonian. If some or all of the southern sinuous ridges are eskers, they could provide evidence for an additional influence of glacial meltwater in Chukhung crater during the mid-to-late Amazonian. If wet-based glaciation did occur in Chukhung crater, the location of the crater between major branches of the Tempe Fossae tectonic rift system would add to the growing body of evidence that elevated geothermal heat flux was an important driver of localized occurrences of recent wet-based glaciation on Mars.

* Corresponding author.
E-mail address: f.butcher@sheffield.ac.uk (F.E.G. Butcher).
[1] Current address: Department of Geography, The University of Sheffield, Sheffield S10 2TN, UK.

1. Introduction

Evidence for past melting of putative debris-covered glaciers (viscous flow features, VFFs) in Mars' mid-latitudes is extremely rare. Recently, however, candidate eskers have been identified in association with two late-Amazonian-aged VFFs in Phlegra Montes (Gallagher and Balme, 2015) and NW Tempe Terra (Butcher et al., 2017, 2020). Eskers are sinuous ridges of glaciofluvial sediment deposited by meltwater draining through tunnels within glacial ice.

The locations of the Phlegra Montes and NW Tempe Terra eskers
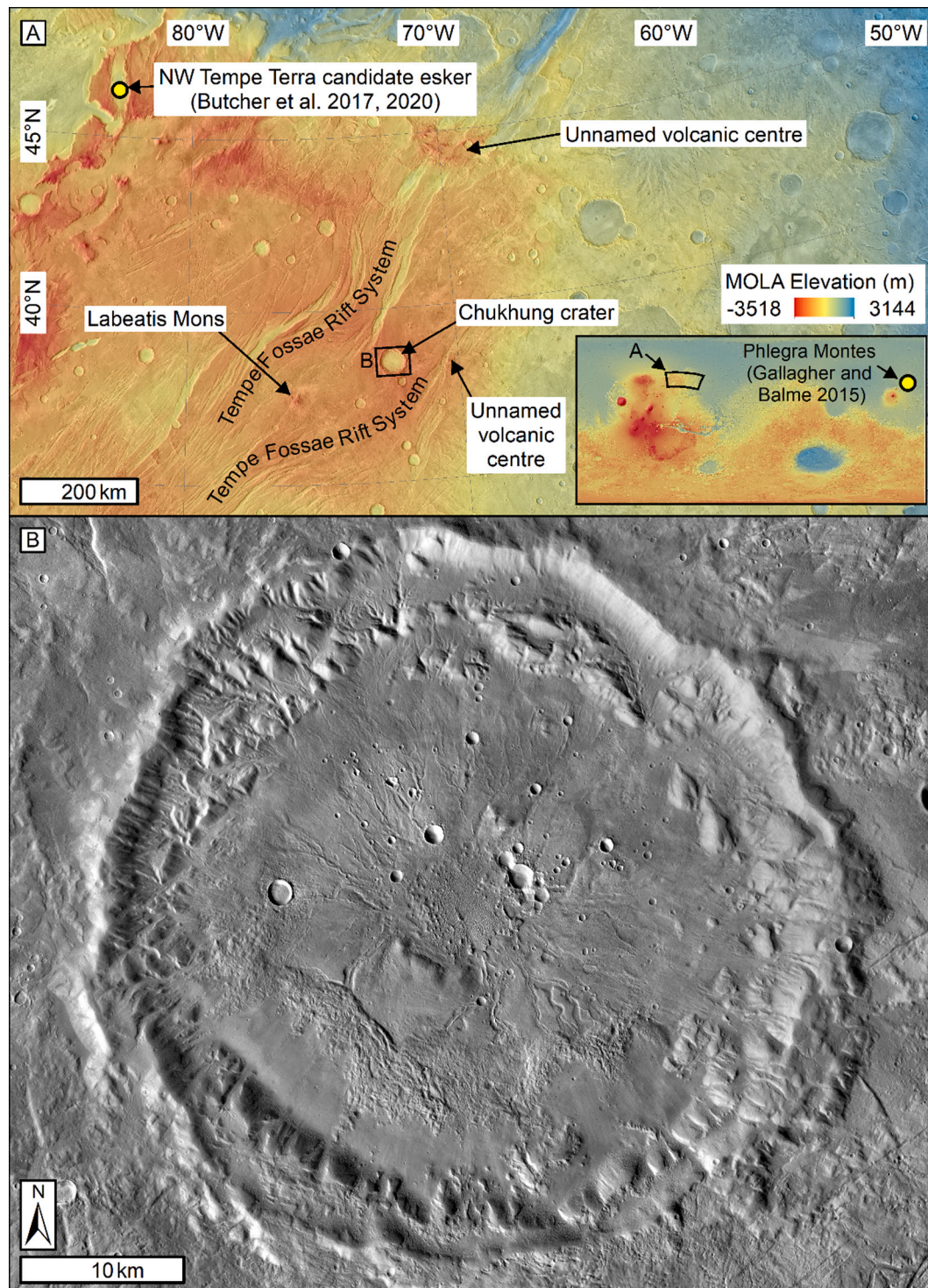
Fig. 1. Location of Chukhung crater. (A) Thermal Emission Imaging System (THEMIS; Christensen et al., 2004; Edwards et al., 2011) daytime infrared image mosaic overlain by colorized Mars Orbiter Laser Altimeter (MOLA; Smith et al., 2001) elevation map of central Tempe Terra (location A in inset global MOLA map), showing the location of Chukhung crater relative to major fault branches and volcanic centers of the Tempe Fossae rift system. Yellow points show locations of candidate glacier-linked eskers previously studied by Butcher et al. (2017, 2020) in NW Tempe Terra, and by Gallagher and Balme (2015) in Phlegra Montes. (B) Context camera image mosaic of Chukhung crater. Extent shown in panel A. See Table S1 for a list of data products. (For interpretation of the references to color in this figure legend, the reader is referred to the web version of this article.)

within tectonic rift/graben valleys supports the hypothesis that localized geothermal heating, possibly accompanied by viscous strain heating within the basal ice, was a prerequisite for the production of glacial meltwater under cold late-Amazonian climate conditions (Gallagher and Balme, 2015; Butcher et al., 2017). Recent modeling experiments exploring the environmental conditions required to explain a possible present-day subglacial lake beneath Mars' south polar ice cap (Orosei et al., 2018) also conclude that above-average geothermal heat flux is required for basal melting (Arnold et al., 2019; Sori and Bramson, 2019).

In order to explore the geothermal hypothesis further, and to constrain the possible extent of wet-based glaciation on Amazonian Mars, it is necessary to search for additional candidate eskers associated with extant VFFs elsewhere on Mars. In this study, we present Chukhung crater in central Tempe Terra (38.47°N, 72.42°W; Fig. 1) as a new site of interest in this search. Chukhung crater hosts sinuous ridges with many esker-like characteristics, which emerge from extant, mid- to late-Amazonian-aged VFF. However, it also hosts landforms interpreted as inverted fluvial paleochannels, which could cast doubt on the origin of the VFF-linked ridges as eskers because of the issue of convergence of form (whereby different processes produce landforms with similar morphologies) between inverted paleochannels and eskers (e.g., Burr et al., 2009). Inverted paleochannels are ridges which preserve fluvial channels in positive relief; they form when channel-fill deposits develop greater resistance to erosion than the adjacent valley floor and/or sides (e.g., by chemical induration and/or armoring), and are exhumed by preferential erosion of those neighboring materials (Maizels, 1987; Pain and Oilier, 1995; Williams et al., 2007, 2013). Unlike eskers, their formation does not require glaciation or glacial meltwater.

We present geomorphic analysis of landforms within Chukhung crater, which is early Hesperian to early Amazonian in age. We draw inferences about the processes that have modified its interior, including fluvial, glacial, and possibly glaciofluvial processes. However, we demonstrate that the interpretation of glacier-linked sinuous ridges in southern Chukhung crater as eskers, and hence the possibility that glaciers in Chukhung crater produced meltwater, is cast into doubt by their coexistence with inverted paleochannels. We do, however, identify one population of sinuous ridges in southern Chukhung crater which is better explained under the esker hypothesis than under the inverted paleochannel hypothesis. Chukhung crater provides a cautionary tale that should be considered during the search for eskers elsewhere on Mars.

Regardless of whether the sinuous ridges are eskers or inverted paleochannels, however, we demonstrate that Chukhung crater has undergone multiple episodes of modification by liquid water since its formation between the early Hesperian and early Amazonian (~3.6–2.1 Ga), and possibly as recently as the mid- to late-Amazonian when environmental conditions on Mars are generally thought to have been extremely cold and hyper-arid.

2. Study location: Chukhung crater

Chukhung crater (38.47°N, 72.42°W) is a ~45 km diameter, ~2.3 km deep impact crater in central Tempe Terra (Fig. 1). It is within the same physiographic region as the tectonic rift valley in NW Tempe Terra that hosts the candidate glacier-linked esker identified by Butcher et al. (2017), which is ~600 km to the northwest. Chukhung crater is located between major grabens within the southwestern segment of the Tempe Fossae rift system (Hauber and Kronberg, 2001), and ~150 km ENE of the central construct of Labeatis Mons. Labeatis Mons is a ~200 km diameter, late-Hesperian-aged (3.51 Ga; Hauber and Kronberg, 2001) volcano which formed during late-stage rifting in Tempe Fossae, and was probably active after major rifting ceased (Hauber and Kronberg, 2001; Hauber et al., 2010). A second, smaller volcanic construct is located within a swarm of grabens ~70 km east of Chukhung crater (Fig. 1A).

3. Aims

We present a geomorphic map of Chukhung crater and explore hypotheses for the formation of its interior units and landforms. In particular, we explore the origins of sinuous ridges that occupy two different portions of the crater floor: (1) sinuous ridges on the southern portion of the crater floor that are spatially associated with (and commonly emerge from beneath) VFF-terminal deposits, and (2) sinuous ridges that extend across the northern portion of the crater floor where there is no discernible evidence for past or present glaciation.

We first consider the hypotheses that: (1) the VFF-linked ridges on the southern portion of the crater floor are eskers, and (2) that the sinuous ridges on the northern portion of the crater floor are inverted paleochannels of non-glacial origin. We then discuss various alternative hypotheses for the origins of the sinuous ridges: (1) that both populations of sinuous ridges in Chukhung crater are eskers, (2) that both populations are inverted paleochannels which pre-date the present glaciation of Chukhung crater, or (3) that the northern and southern sinuous ridge populations contain mixtures of eskers and inverted paleochannels, and thus that the formation mechanisms cannot be divided on a north-south basis. In considering the alternative formation hypotheses for the sinuous ridges, we highlight some of the challenges that remain for the ongoing search for eskers on Mars. Finally, we consider the implications of the sinuous ridges for the history of fluvial, glacial, and glaciofluvial activity in Chukhung crater.

## 4. Data and methods

4.1. Observations and mapping

We produced a geomorphic map of the interior of Chukhung crater using a basemap comprising ~6 m/pixel Context Camera (CTX; Malin et al., 2007) images (listed in Table S1), which provide complete coverage of the mapping area (Fig. 2). We supplemented our analyses with seven High Resolution Imaging Science Experiment (HiRISE; McEwen et al., 2007) images (six of 25 cm/pixel, and one of 50 cm/pixel horizontal resolution), which provide partial coverage of the mapping area (Fig. 2). We integrated these image data with: (1) a single 75 m/pixel High Resolution Stereo Camera (HRSC; Neukum et al., 2004; Jaumann et al., 2007) digital elevation model (DEM), which provides complete coverage of the mapping area (Fig. 2, Table S1); (2) a 24 m/pixel DEM derived from two CTX images by Mayer and Kite (2016), which provides coverage of the western two-thirds of the mapping area; and (3) a 1 m/pixel HiRISE DEM generated by the same authors (Mayer and Kite, 2016), which provides coverage of a portion of the central crater floor (see Table S1 for a complete list of data products, and Fig. 2 for a map of data coverage). To minimize cartographic distortion, we digitized the map in a sinusoidal projection centered on 72.5°W using ESRI ArcGIS 10.1 software.

We identified map units based on visual similarities in their surface morphologies. We identified contacts between map units based on changes in surface morphology and/or differences in unit emplacement ages evidenced by superposition relationships.

4.2. Age estimations from impact crater size-frequency distributions

We measured size-frequency distributions of impact craters to estimate: (1) an approximate envelope for the age of Chukhung crater itself, and (2) the minimum age of the VFF within Chukhung crater. We measured crater size-frequency distributions on the CTX image basemap using the *CraterTools* add-in for ArcGIS (Kneissl et al., 2011).

The interior of Chukhung crater has been subject to significant post-impact modification such that impact crater populations within it would not provide a reliable estimation of the age of the Chukhung-forming impact. Additionally, the ejecta blanket of Chukhung crater is thin and indistinct such that age determinations based on the size-frequency
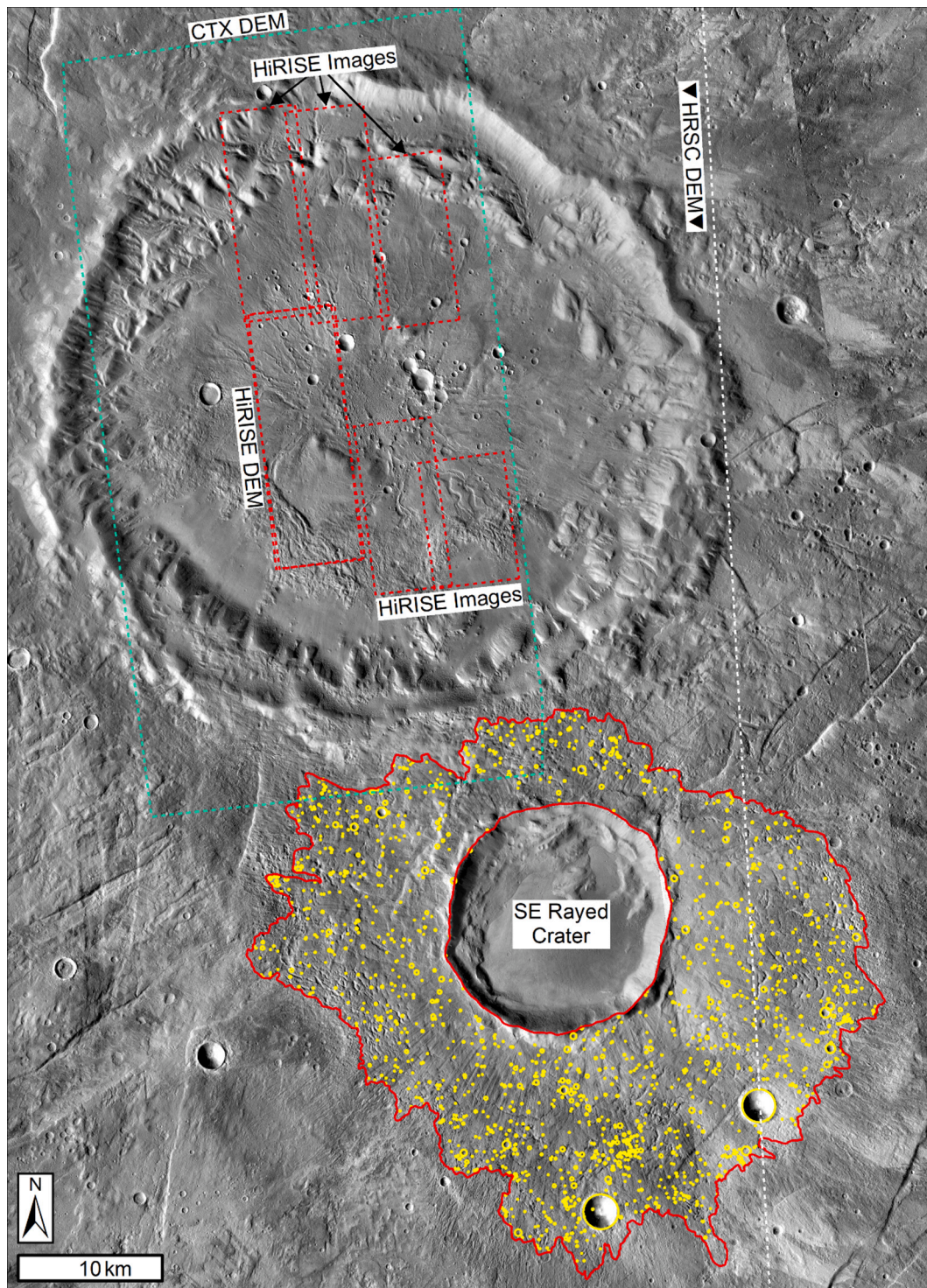
Fig. 2. Data coverage of Chukhung crater and the rayed impact crater to the SE. The CTX image basemap provides complete coverage of the study area. Dashed boxes show extent of: 7 HiRISE images (red), including a stereo pair from which Mayer and Kite (2016) produced a digital elevation model; the CTX DEM (blue) from Mayer and Kite (2016); and the HRSC DEM (white dashed line shows easternmost extent). The solid red line shows the area of the impact ejecta of the SE rayed crater for which we obtained impact crater size-frequency statistics. Yellow circles are counted impact craters with diameters ≥ 70 m. See Table S1 for data products. (For interpretation of the references to color in this figure legend, the reader is referred to the web version of this article.)

distribution of impact craters upon it would be unreliable. Therefore, we constrained an approximate envelope for the age of Chukhung crater itself based on the modeled ages of units that underlie and superpose it in the regional stratigraphy. We compared the estimated age of the early-Hesperian volcanic unit (eHv; Tanaka et al., 2014a), upon which it is superposed, with new measurements of the size-frequency

distribution of impact craters on the better-preserved ejecta of a ~ 15 km diameter rayed crater, which superposes the southeastern rim of Chukhung crater (hereafter referred to as the 'SE rayed crater'; Fig. 2). The age estimate for the early-Hesperian volcanic unit by Tanaka et al. (2014a) is based upon the size-frequency distribution of impact craters on a reference surface in Icaria Planum centered on 105.96°W, 41.92°S.

We measured all un-deformed impact craters of diameter (D) ≥ 70 m on the surface of the ejecta blanket of the SE rayed crater (Fig. 2). The decameter-scale relief of the rayed ejecta made identification of impact craters with $D < 70$ m unreliable.

To estimate a minimum age for the VFF in Chukhung crater, we measured all un-deformed impact craters of $D \geq 50$ m on their surfaces. Impact craters with $D < 50$ m could not be distinguished reliably from pits on the VFF surfaces.

We identified potential for a significant influence of secondary impact craters from the SE rayed crater upon the measured impact crater
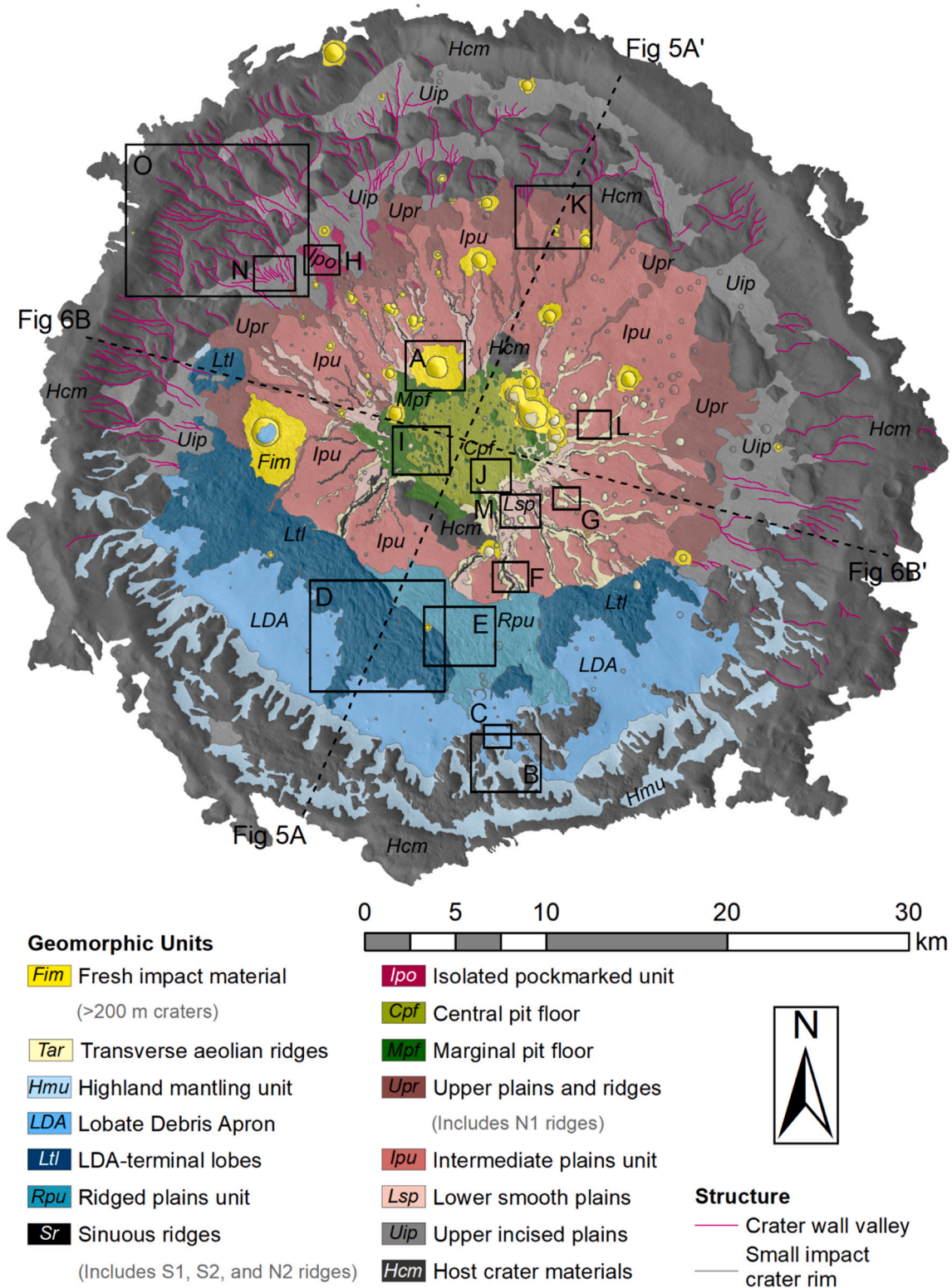

Fig. 3. Geomorphic map of Chukhung crater. Boxes show extents of panels in Fig. 4, and dashed lines show locations of profiles in A–A′ and B–B′ in Figs. 5 and 6, respectively. Map overlain on CTX image mosaic (see Table S1). See Fig. S1 for enlarged map. (For interpretation of the references to color in this figure legend, the reader is referred to the web version of this article.)

size-frequency distributions. Therefore, we performed spatial randomness analyses on the measured impact crater populations using the randomness analysis tool in *CraterStats2* (Michael et al., 2012). We produced 3000 random spatial distributions of an impact crater population with the same characteristics as the measured population. Following Michael et al. (2012), we then compared the mean second closest neighbor distance (M2CND) of the measured population (for various ranges of impact crater diameters) to those of the simulated populations (over the same diameter range). For diameter ranges in which the true M2CND fell within one standard deviation of the mean simulated M2CND, we considered crater distributions to be spatially random. For impact crater diameter ranges in which the true M2CND deviated from the mean simulated M2CND by more than one standard deviation, we considered impact craters to be non-randomly distributed. Where this was true, we considered contamination of the impact crater population by secondary impact craters to be important and approached interpretation of modeled ages with greater caution. Secondary impact craters artificially increase the modeled age of an affected surface. Spatially heterogeneous resurfacing processes can also cause spatial clustering. In contrast to secondary cratering, resurfacing destroys impact craters, resulting in underestimation of model ages from impact crater size-frequency distributions.

5. Observations

Our geomorphic map of Chukhung crater is displayed in Fig. 3, and example images of mapped units are displayed in Fig. 4. An enlarged version of the map is provided in Supplementary Fig. S1. Chukhung crater is ~45 km in diameter and ~2.3 km deep. It has multiple crater wall terraces, and a ~ 10.7 km diameter, ~225 m deep central floor pit (Robbins and Hynek, 2012). The rim of the central pit has variable topographic expression (Figs. 5 and 6). Steep scarps separate the NE and SW margins of the central pit from the crater floor above (Fig. 6), whereas the NW and eastern margins of the central pit are topographically indistinct; topographic profiles from the crater rim to the floor of the central pit in these locations (e.g., Fig. 6) are broadly concave. The floor of Chukhung crater has undergone significant post-impact modification. It hosts various geomorphic units (Figs. 3–6), which we now describe.

5.1. Lobate debris aprons and Highland mantling units

Deposits with pitted and lineated surface textures, consistent with lobate debris apron (LDA) type VFFs (Squyres, 1979; Head et al., 2010), extend up to 5 km across the floor of Chukhung crater from the W–SE portions of the crater wall (Figs. 3, 4C, 5, and 8A). LDAs are widely considered to be analogous to debris-covered glaciers (e.g., Holt et al., 2008; Plaut et al., 2009; Petersen et al., 2018). Topographic profiles oriented from the headward margins to the termini of LDAs in Chukhung crater are predominantly convex-up (Fig. 5), though in some areas they are concave. At their headward margins, the LDA surfaces transition gradationally to a highland mantling unit (*Hmu* in Fig. 3), similar to that interpreted as ice-rich highland mantling in NW Tempe Terra by Butcher et al. (2017). The highland mantling unit has a lineated texture and infills topographic lows in the southern crater wall, including wide (hundreds of meters), low-sinuosity crater wall valleys, and the upper surfaces of crater wall terraces (Figs. 3, 4B, 5, and 6).

We do not observe similar ice-rich LDAs or highland mantling deposits on the northern or eastern portions of the crater floor or wall (Figs. 3–6).

5.2. LDA-terminal lobes and ridged plains units

The termini of the LDAs in Chukhung crater are bounded by prominent lobate ridges (LDA-terminal lobes, *Ltl*) comprising hummocky deposits and concentric parallel ridges (Figs. 3, 4D, and 8). The lobes are oriented parallel to the LDA termini and extend 2–5 km across the southern crater floor. LDA materials infill topographic depressions in the upper margins of the LDA-terminal lobes (Fig. 8), whereas the steep lobe-frontal margins have tens of meters (up to ~100 m) of relief (Fig. 5). Two ~2 km wide gaps exist in the lobate deposits at the termini of the north-facing LDAs (Figs. 3 and 8). In these zones, the LDA termini transition to low-relief hummocky plains (Figs. 4E, 5, and 8A) comprising heterogeneous undulatory forms which superpose numerous parallel, NNW-oriented lineae with lengths of hundreds of meters (Fig. 4E). The LDA-terminal lobes and ridged plains units occur only on the southern and western portions of the crater floor.

### 5.3. Southern sinuous ridges and crater-floor valleys in intermediate plains

The southern floor of Chukhung crater hosts 16 sinuous ridge systems (Figs. 8 and 9A, B, E, F), five of which emerge from beneath the LDA-terminal lobes and ridged plains units (e.g., Figs. 8A and D, and 9A). They extend several kilometers towards the margins of the crater's central pit. Superposition relationships (e.g., Fig. 9E) suggest that at least two stratigraphically-distinct sets of sinuous ridges exist on the southern crater floor: a stratigraphically-lower set of ridges (hereafter referred to as S1 ridges; Fig. 9A), and a stratigraphically-higher set of ridges (hereafter referred to as S2 ridges; Fig. 9B). The S1 ridges (n = 7) have typical lengths of ~1.4–4 km and typical sinuosities of ~1.1–1.2. The S2 ridges (n = 9) have typical lengths of <1–4 km and typical sinuosities of ~1–1.6. Thus, the S2 ridges are typically more sinuous than the S1 ridges.

Based on visual interpretation of crest morphologies from CTX and HiRISE images, the S1 ridges are predominantly sharp- to round-crested, but ~40% of S1 ridges also have flat-topped sections. The S1 ridge with HiRISE DEM coverage (Fig. 9A) has a typical height of ~10–20 m and a typical width of ~150–300 m. The S2 ridges are sharp-crested. Those with HiRISE DEM coverage (e.g., Fig. 9B) are generally lower and narrower than S1 ridges, having typical heights of ~7–10 m, and widths of ~100–150 m.

The S1 ridges occupy broad crater floor valleys which have widths of hundreds of meters and depths of tens of meters (e.g., Figs. 4F, 8, and 9A). The valleys extend across the intermediate plains unit (*Ipu*; Fig. 3, 4L, and 9A). The intermediate plains unit is a low-relief, crater-concentric plains unit which dominates the crater floor (Fig. 3). The intermediate plains unit has a somewhat smooth appearance in southern Chukhung crater and is comparatively rugged in the north (see Section 5.4). In contrast to the S1 ridges, the S2 ridges do not conform to the axes of the crater floor valleys incised into the intermediate plains unit. Four S2 ridges ascend the walls of those valleys and escape over the lateral valley margins to cross onto the adjacent plateaus of the intermediate plains unit (Figs. 8B–C). One S2 ridge crossing the intermediate plains is not hosted within a crater floor valley (Fig. 9B). Five S2 ridges superpose S1 ridges, tracking along, or crossing over, their crests (Fig. 9E). In two locations, S2 ridge systems form quasi-dendritic networks (Figs. 3 and 9E). In at least one location, an S1 ridge does not appear to follow the central axis of its host valley, appearing to locally ascend and then descend the valley wall; however, the ridge does not cross out of the valley at any point along its length (Fig. 8D).

The valleys within which many of the southern sinuous ridges are located are consistently deeper than the heights of the ridges themselves. While seven crater floor valleys emerge from beneath the LDA-terminal lobes or ridged plains units (Fig. 8), nine similar (though visibly shallower) valleys on the SE and E floor do not (Fig. 3). Sinuous ridges are uncommon, but not absent, within the valleys on the SE and E floor. The valley floors are largely obscured by transverse aeolian ridges (TARs; Fig. 4G; Balme et al., 2008). TARs also occur on the floors of many small impact craters on the southern and eastern floor of Chukhung crater (Figs. 3 and 4G). Where they coexist with sinuous ridges, TARs superpose the flanks and crests of those ridges. The heads of the
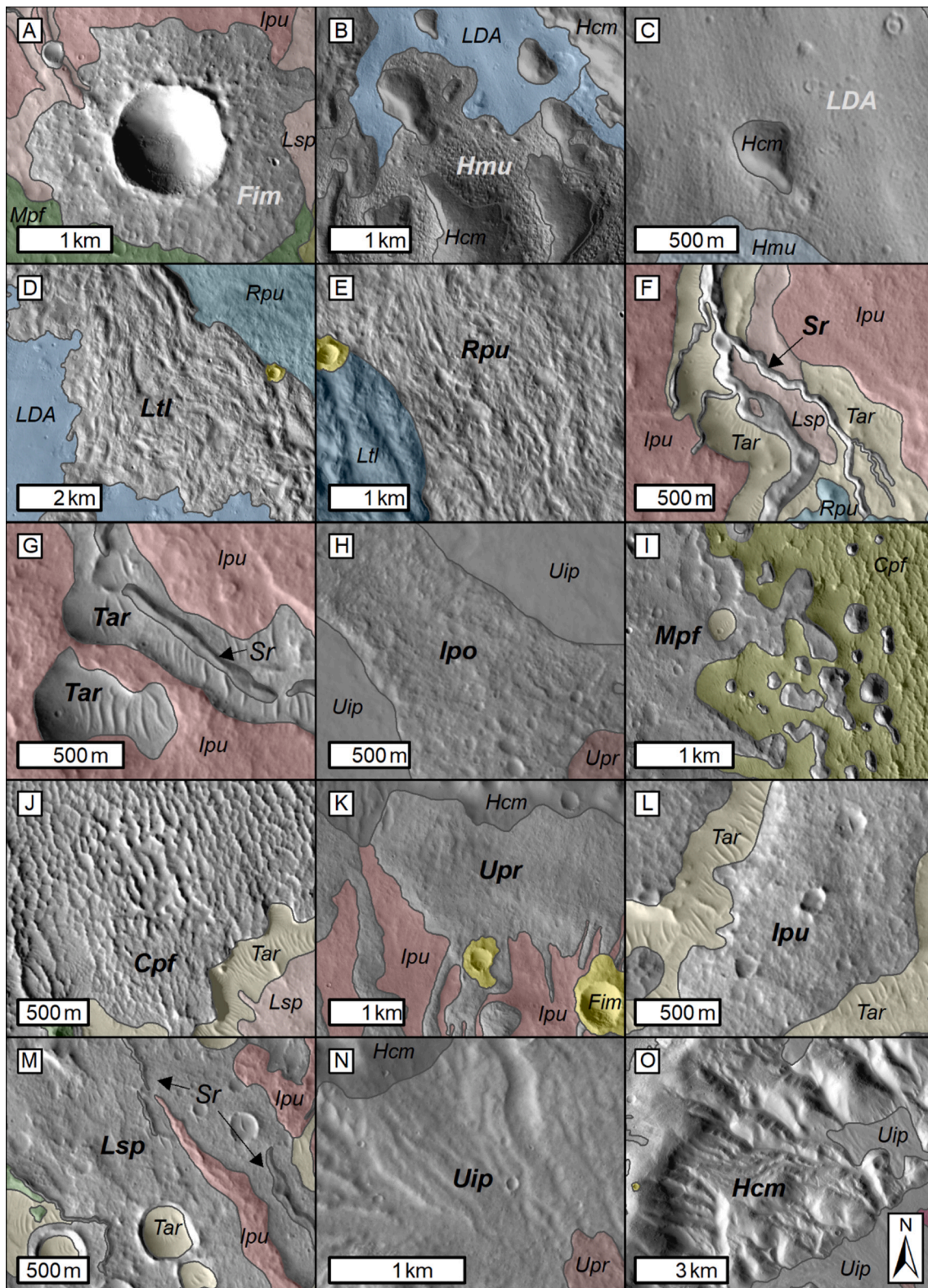
Fig. 4. CTX images of geomorphic units in Chukhung crater. For clarity, contextual units are colorized, but the subject unit of each panel (with unit label emboldened) is not. See Fig. 3 for extents and legend. (A) Fresh impact material, *Fim*. (B) Highland mantling unit, *Hmu*. (C) Lobate Debris Apron, *LDA*. (D) LDA-terminal lobes, *Ltl*. (E) Ridged plains unit, *Rpu*. (F) Sinuous ridges, *Sr*. (G) Transverse aeolian ridges, *Tar*. (H) Isolated pockmarked unit, *Ipo*. (I) Marginal pit floor unit, *Mpf*. (J) Central pit floor, *Cpf*. (K) Upper plains and ridges unit, *Upr*. (L) Intermediate plains unit, *Ipu*. (M) Lower smooth plains, *Lsp*. (N) Upper incised plains, *Uip*. (O) Host crater materials, *Hcm*. See Table S1 for data products. (For interpretation of the references to color in this figure legend, the reader is referred to the web version of this article.)
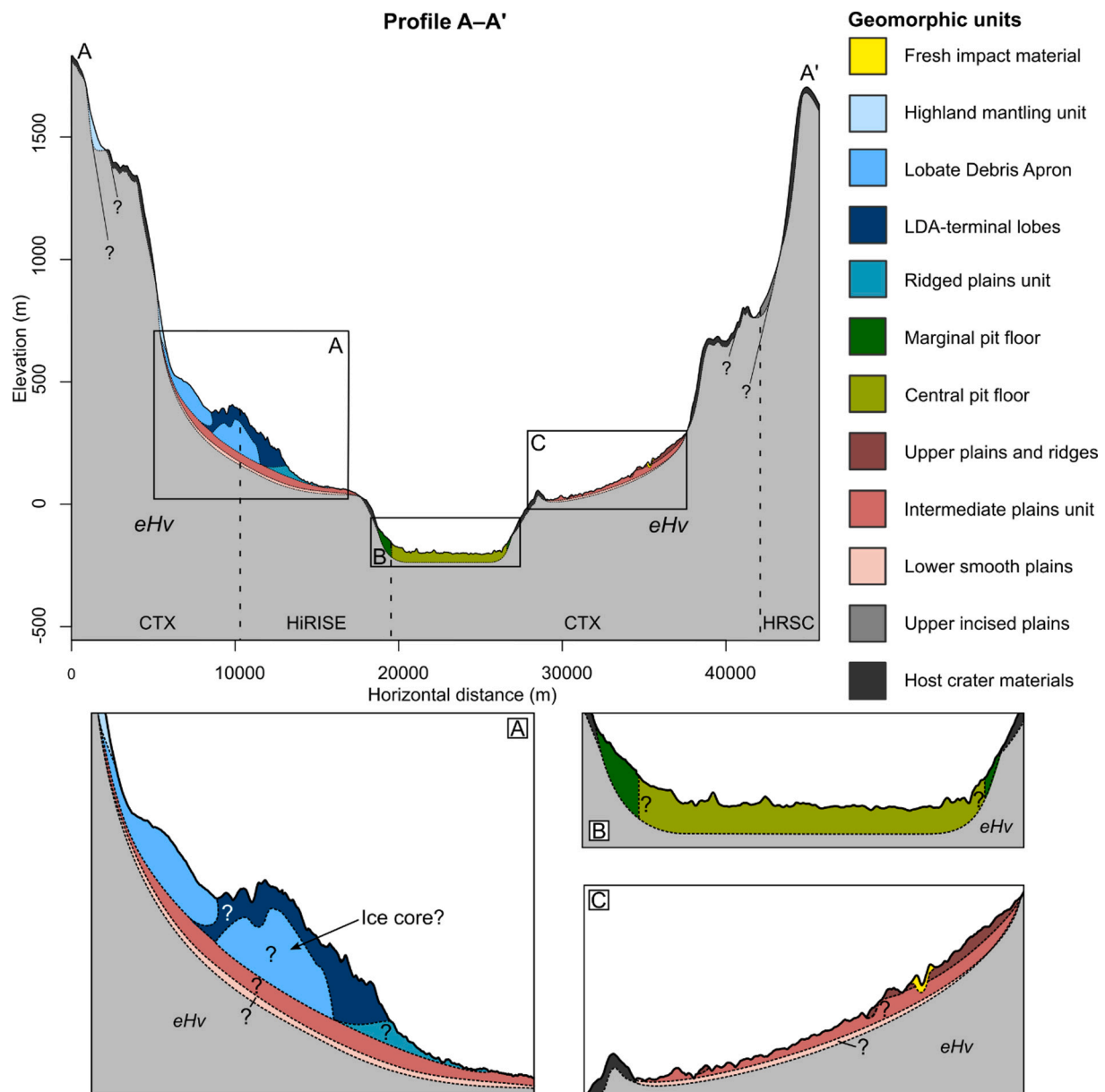
Fig. 5. Schematic cross-section A–A′, showing inferred stratigraphic relationships between mapped units in Chukhung crater. Location of profile is shown in Fig. 3. The upper solid line is topography from CTX, HiRISE, and HRSC DEMs at 15 times vertical exaggeration (dashed lines show DEM extents, see Table S1 for data products), and all contacts below this line have inferred depths and profiles. Boxes show extents of enlarged inset views A, B, and C. eHv is the early-Hesperian volcanic unit (Tanaka et al., 2014a, 2014b). In this topographic profile, the crater's central pit has topographically-prominent margins. (For interpretation of the references to color in this figure legend, the reader is referred to the web version of this article.)

valleys on the SE and E floor (and additionally the northern floor; See Section 5.4) commonly emerge from beneath sinuous, finger-like extensions of a smooth plains unit (upper plains and ridges, *Upr*) which appears to superpose the upslope margins of the intermediate plains unit (Figs. 3, 4K, 5, and 6). The surface texture of the upper plains and ridges unit is similarly smooth and low-relief to the intermediate plains unit; however, the upper plains and ridges unit forms positive-relief ridges extending from its downslope margins, whereas the intermediate plains unit is valley-incised and does not appear to form positive relief features.

The downslope termini of the southern crater floor valleys are indistinct; they open out onto a smooth plains unit (lower smooth plains, *Lsp*) which extends from low-relief contacts at the lower margins of the intermediate plains unit, to the margins of the central pit (Figs. 3 and 4M). The lower smooth plains have a more rugged surface texture than the intermediate plains unit, and are primarily defined based on

stratigraphic position below the intermediate plains unit.

5.4. Northern sinuous ridges, crater floor valleys, and upper plains

The northern portion of the floor of Chukhung crater also hosts assemblages of sinuous ridges and valleys. As on the southern floor, valleys occur within the intermediate plains unit, and expose lower smooth plains on their floors (Figs. 7 and 9C). However, in this portion of the crater floor, the valley walls are less visually distinct (being more easily identifiable in topographic profiles than in images), and the surrounding intermediate plains unit has a more rugged and degraded texture than it has on the southern floor (Figs. 10A and 11).

Some of the northern crater floor valleys appear to be longitudinally discontinuous, though the ejecta of numerous superposed impact craters obscures their relationships to downslope valley segments (Figs. 3 and
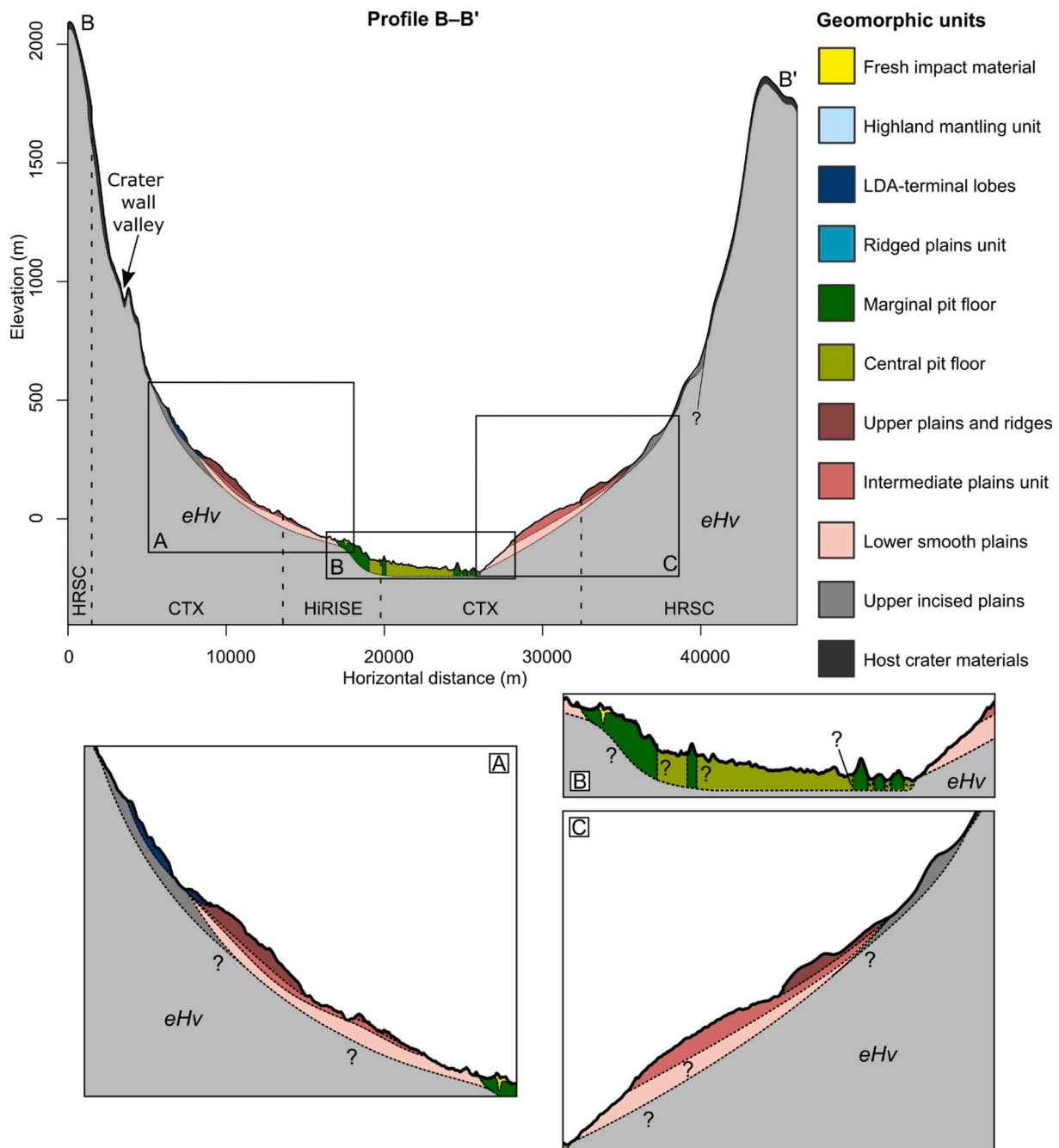
Fig. 6. Schematic cross-section B–B′, showing inferred stratigraphic relationships between mapped units in Chukhung crater. Location of profile is shown in Fig. 3. The upper solid line is topography from CTX, HiRISE, and HRSC DEMs at 15 times vertical exaggeration (dashed lines show DEM extents, see Table S1 for data products), and all contacts below this line have inferred depths and profiles. Boxes show extents of enlarged inset views A, B, and C. *eHv* is the early-Hesperian volcanic unit (Tanaka et al., 2014a, 2014b). In this profile, the NW margin of the central pit is not topographically prominent, resulting in a broadly concave profile from the NW crater wall to the center of the crater. (For interpretation of the references to color in this figure legend, the reader is referred to the web version of this article.)

9C). Unlike in the southern portion of the crater, the valley floors are unobscured by TARs. Similarly to the valleys on the SE and E portions of the crater floor, the northern crater floor valleys commonly emerge from beneath finger-like extensions of the smooth upper plains and ridges unit (Figs. 3, 4K, 10). On the northern floor, many (though not all) of these finger-like features are continuous or aligned with sinuous ridge systems (hereafter referred to as N1 ridges, n = 18, Figs. 9C, 10, 11), whose paths appear largely to conform to the axes of the valleys within which they occur (Fig. 9C). Approximately 20% of the sinuous ridges that extend from the upper plains and ridges unit are not clearly associated with

crater floor valleys (Fig. 10B).

The N1 ridges have typical lengths of ∼ 1–7.5 km and typical sinuosities of ∼1–1.2. They have more variable crest morphologies (including sharp-crested, round-crested, multi-crested, and flat-topped) and more rugged surface textures than other sinuous ridges in Chukhung crater (Figs. 10 and 11). They have variable topographic expression, ranging from prominent ridges to low-relief features. In locations with HiRISE and CTX DEM coverage, prominent ridge portions have typical heights of ∼5–20 m and typical widths of ∼150 m–1.1 km.

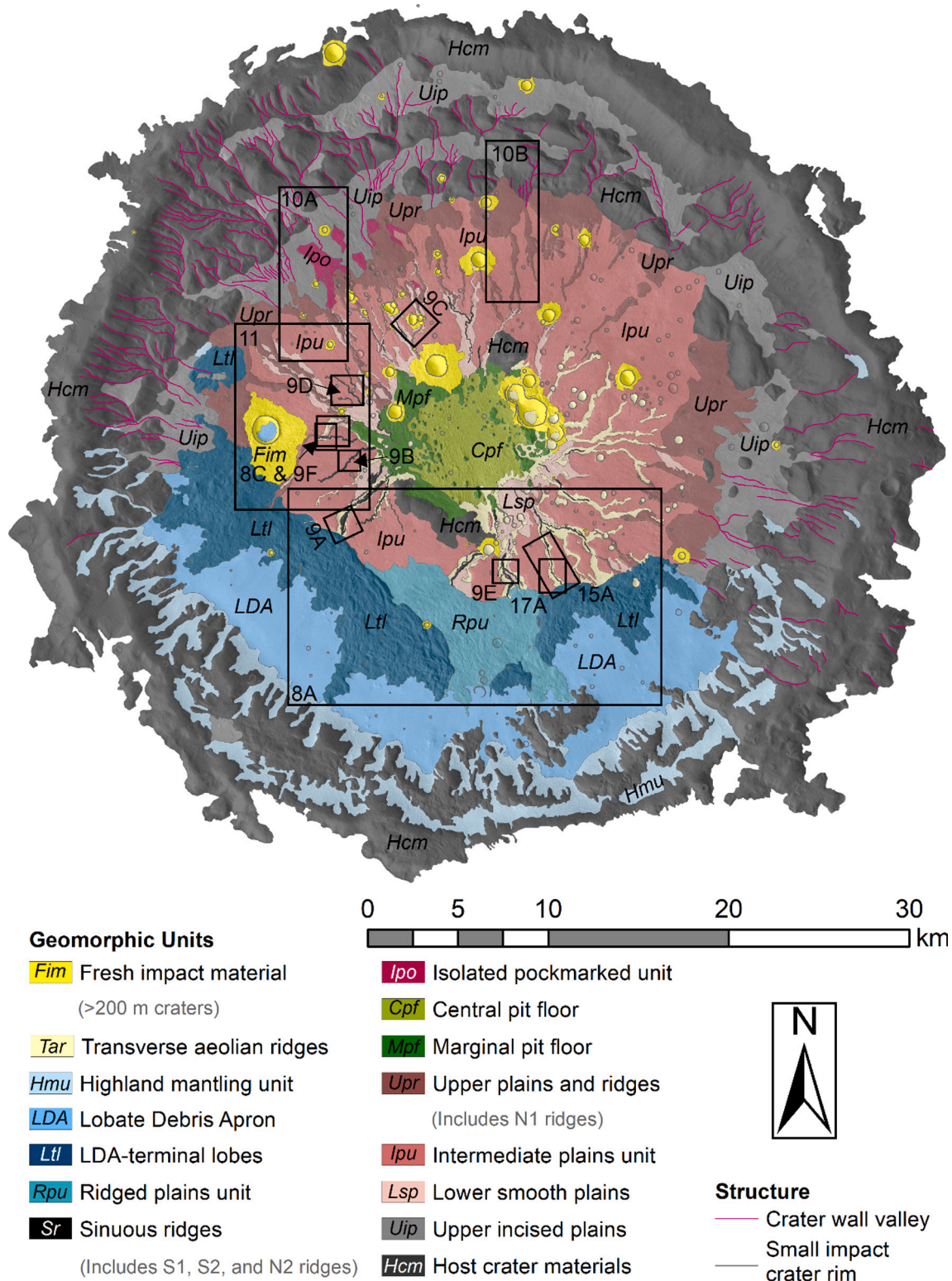A notable N1-type sinuous ridge network occurs on the WNW portion

Fig. 7. Geomorphic map of Chukhung crater showing extents of subsequent figures. See Fig. S1 for enlarged map. (For interpretation of the references to color in this figure legend, the reader is referred to the web version of this article.)

of the crater floor (Fig. 11). It is flat-topped, and has multiple branches that extend from the upper plains unit to the NW. Another branch emerges from beneath the LDA-terminal lobe unit to the SW. The SW branch may once have merged with the NW branch close to the margins of the crater's central pit, but their relationship is obscured by a more recent impact crater (Fig. 11). The portion of the upper plains and ridges

unit from which the NW branch emerges appears to be layered (Fig. 11, white arrows). Two of the NW branches appear to form an anabranching network morphology, but close inspection suggests that the branches could be at different stratigraphic levels (Fig. 11, inset). The SW branch that emerges from the LDA-terminal lobe is superposed by an S2 sinuous ridge, which trends west-to-east across the valley, weaving along
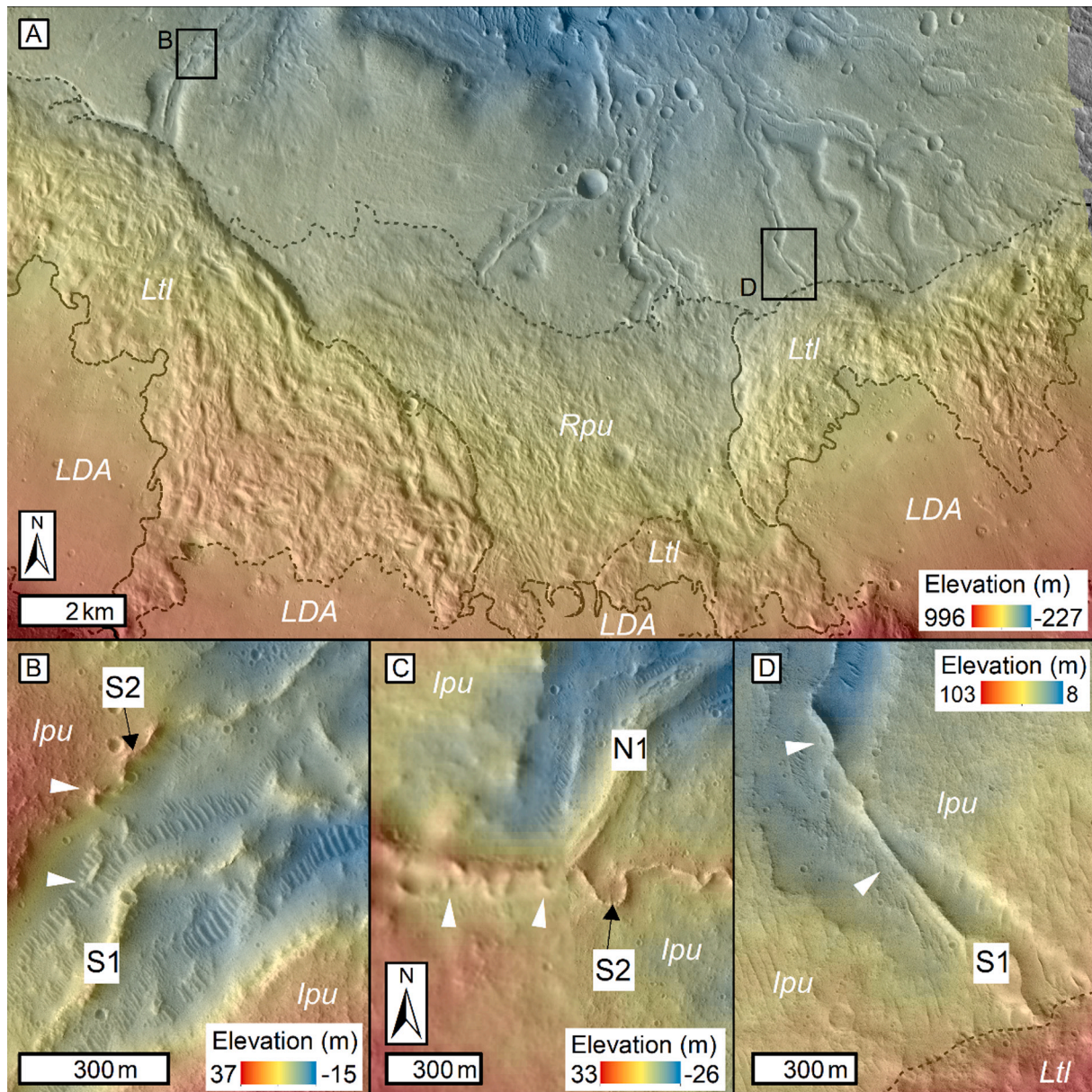
Fig. 8. Landform associations and sinuous ridges on the southern floor of Chukhung crater.(A) CTX image mosaic overlain by 24 m/pixel CTX DEM showing the LDA-terminal lobes (*Ltl*) which bound the LDA termini, the ridged plains unit (*Rpu*) which occupies a gap in the *Ltl*, and the emergence of several of the southern sinuous ridges from beneath these units. Black boxes show the extents of panels B and D. (B) HiRISE image overlain by 1 m/pixel HiRISE DEM showing a sharp-crested S2-type ridge which weaves up and down the wall of a crater-floor valley (between white arrows) occupied by an S1-type ridge. (C) HiRISE and CTX images overlain by 24 m/pixel CTX DEM showing a sharp-crested S2-type ridge superposing the flat-topped crest of the SW branch of the N1-type ridge in Fig. 11 (between white arrows) and ascends out of the crater floor valley and onto the adjacent intermediate plains (*Ipu*). Extent shown in Fig. 7. (D) HiRISE image overlain by 24 m/pixel CTX DEM showing a sharp-crested S1-type ridge which emerges from beneath the LDA-terminal lobe (*Ltl*) unit and appears to ascend then descent the wall of the crater floor valley it occupies (between white arrows) rather than following the strike of the valley floor. See Table S1 for data products. (For interpretation of the references to color in this figure legend, the reader is referred to the web version of this article.)

a ~ 600 m portion of the crest of the N1 ridge before extending eastward across the adjacent intermediate plains unit.

Eleven sharp-crested ridge systems (hereafter referred to as N2 ridges) with very similar morphologies and typical heights and widths to the S2 ridges (Section 5.3) also occur on the northern portion of the floor of Chukhung crater (Figs. 3 and 9D). The N2 ridges have typical sinuosities of 1–2.1. Several N2 ridges are not clearly associated with crater-floor valleys; however, one example comprises two branches which extend along a valley network emerging from beneath a finger-like extension of the upper plains and ridges unit (to the NE of the box demarcating the extent of Fig. 4A in Fig. 3). Unlike the observed relationships between S1 and S2 ridges, none of the N2 ridge systems appear to ascend valley walls or cross the crests of N1 type ridges.

In many locations, the relationship between the northern sinuous ridges and deposits in the central pit are obscured by small impact craters. However, where the N1 type sinuous ridges can be traced to its margins, they appear to grade into central pit deposits.

5.5. Central pit units

As described above, the N-W margins of Chukhung crater's central pit lack topographic expression. Two of the major N1-type sinuous ridge networks that extend across the NW portion of the crater floor appear to transition into a smooth unit which occupies the inner margins of the
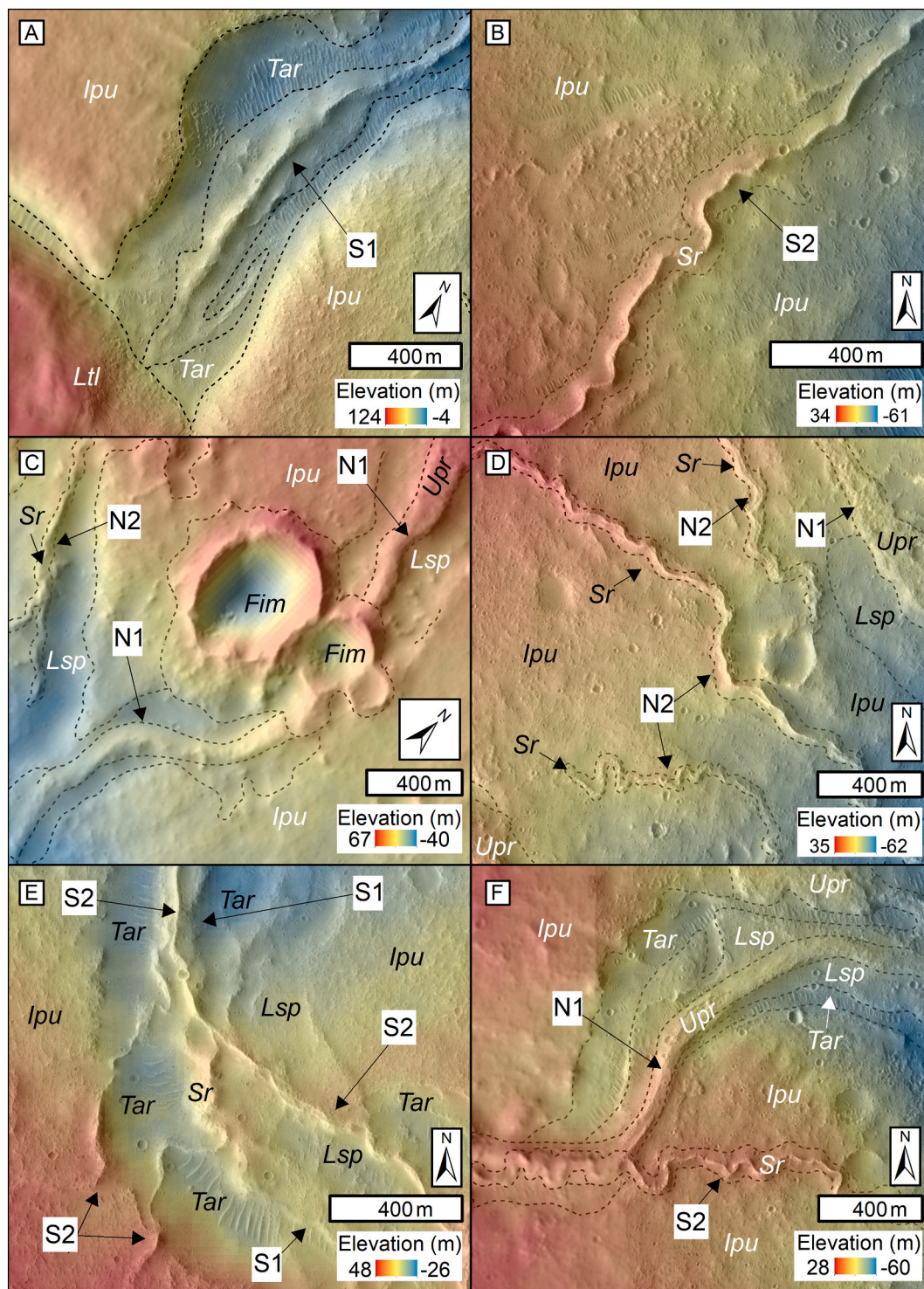
Fig. 9. Sinuous ridges in Chukhung crater. (A) Sharp- to round-crested S1-type sinuous ridge within a valley on the southern floor. (B) Sharp-crested S2-type sinuous ridge crossing the intermediate plains on the southern floor. (C) Flat-topped to round-crested N1-type sinuous ridge within a valley on the northern floor. It is disrupted by fresh impact material. (D) Sharp-crested N2-type ridges crossing plains on the northern floor. (E) Dendritic network of sharp-crested S2-type ridges, which descend into a valley on the southern floor, then ascend the flanks of a flat-topped S1-type sinuous ridge occupying the valley floor, and continue down-valley atop its crest. (F) Sharp-crested S2-type ridge which superposes a flat-topped branch of an N1-type ridge on the south-western floor. The S2 ridge crosses onto a plateau east of the valley. Extents shown in Fig. 7. Panels A–B and D–F are HiRISE images. Panel C and the western portion of panel F are CTX images. Panels A, C, E, and F are overlain by a 24 m/pixel CTX DEM. Panels B and D are overlain by a 1 m/pixel HiRISE DEM. See Fig. 7 for unit abbreviations and Table S1 for data products. (For interpretation of the references to color in this figure legend, the reader is referred to the web version of this article.)
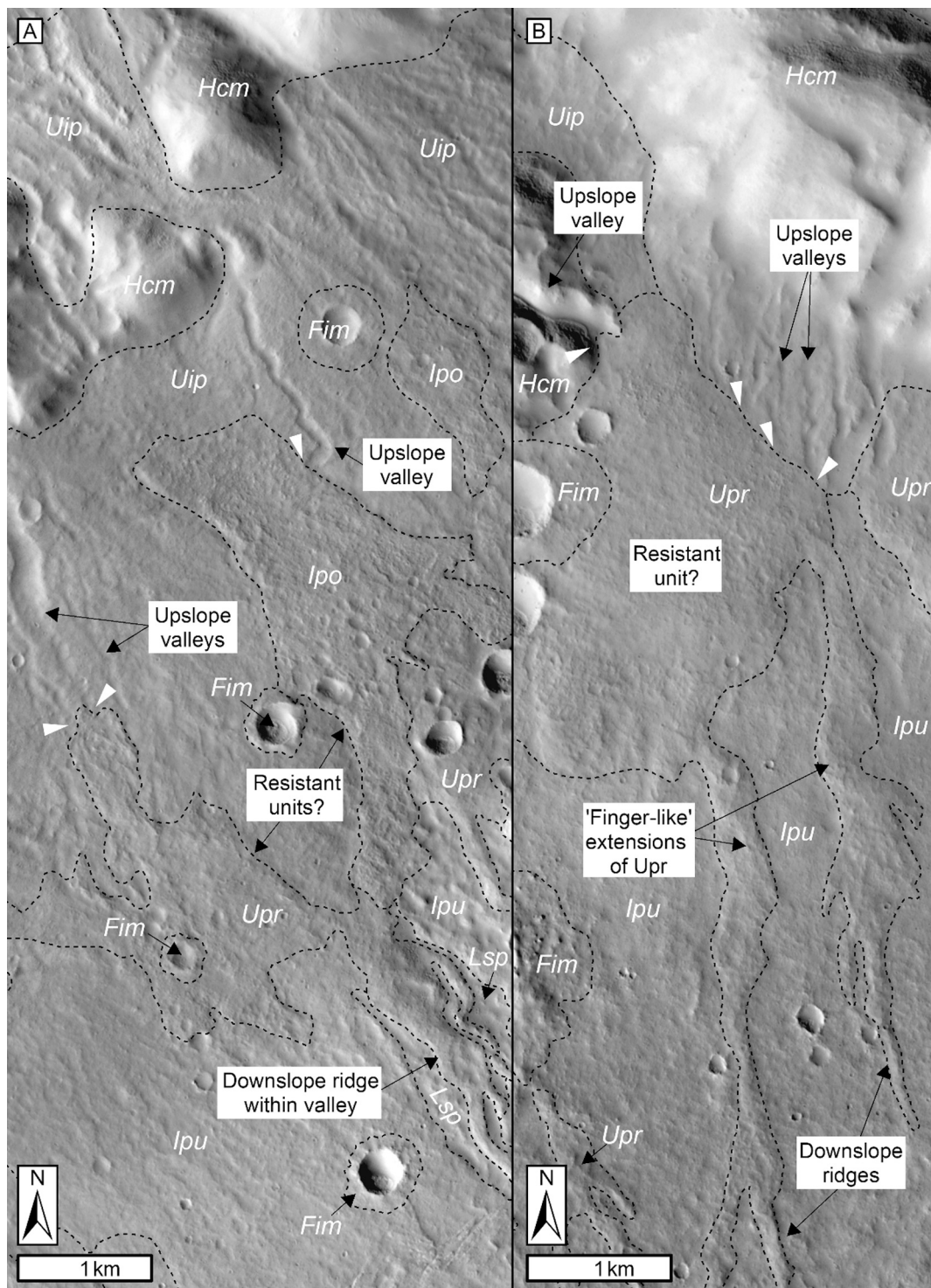
Fig. 10. Relationships between upslope valleys and downslope sinuous ridges in the northern portion of Chukhung crater. (A) CTX image mosaic showing valleys within the Upper incised plains unit, which are superposed (white arrows) by the Upper plains and ridges (*Upr*) and Isolated pockmarked (*Ipo*) units downslope. Associated sinuous ridges extend downslope from the *Upr*. (B) CTX image mosaic showing crater wall valleys superposed by the *Upr* unit, and finger-like extensions from its downslope margins which transition into sinuous ridges. See Table S1 for data products. (For interpretation of the references to color in this figure legend, the reader is referred to the web version of this article.)

central pit (marginal pit floor unit, *Mpf*; Figs. 3, 4I, and 11). The marginal pit floor unit extends unbroken from the northern margin of the central pit, westward around its margins, to the base of the scarp at the SW margin of the central pit (Fig. 3). The surface of the marginal pit floor unit generally slopes towards the SE, but well-preserved portions of its surface have flat tops (Fig. 4I).

The eastern margins of the marginal pit floor unit have tens of meters of relief (Figs. 4I and 6). Numerous outlying flat-topped and rounded mesas of marginal pit floor materials occur beyond the eastern margins of the main deposit, their spatial density reducing towards the center of the central pit (Figs. 3 and 4I). Similar mesas also occur around the NE, W, and S margins of the central pit, and at the terminus of an S1 ridge
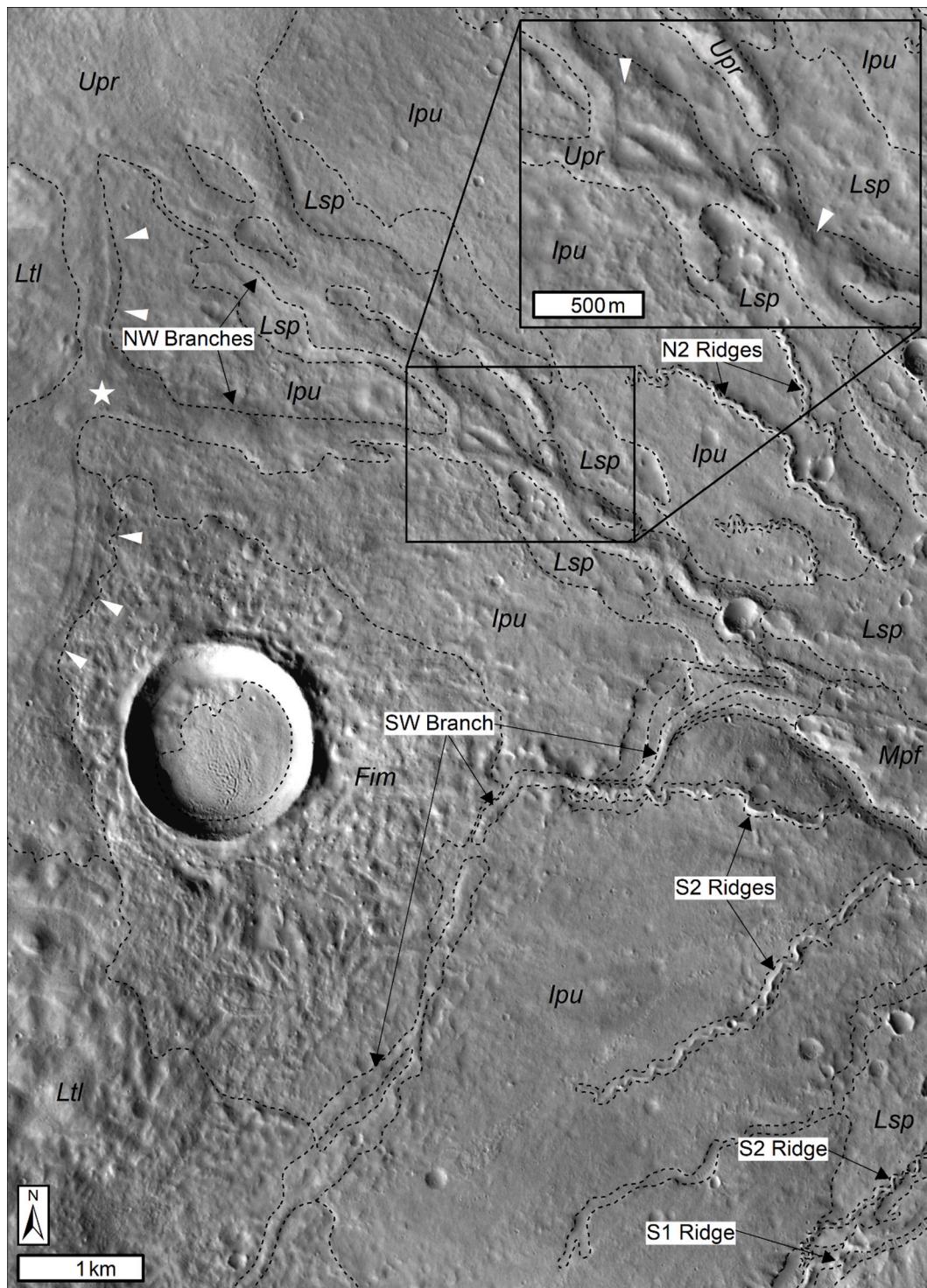
Fig. 11. A prominent N1-type sinuous ridge on the NW floor of Chukhung crater. Key units are labelled (see Fig. 3 for abbreviations). Plains-forming *Upr* materials appear to have internal layering (white arrows) where one of the NW branches emerges (white star). The NW branches might represent an anastomosing paleo-channel network, but subtle elevation differences (white arrows in inset) may instead indicate migratory paleochannel systems at different stratigraphic levels. The SW branch emerges from the LDA-terminal lobe unit and is superposed by a S2-type ridge. CTX image mosaic (see Table S1 for data products). (For interpretation of the references to color in this figure legend, the reader is referred to the web version of this article.)

(Fig. 3).

The mesas of the marginal pit floor unit are surrounded by the unit that dominates the central portion of the central pit: the central pit floor (*Cpf*) unit. The central pit floor is ~30 m lower in elevation than the marginal pit floor unit and hosts a high density of variably-oriented ridges in highly interconnected networks (Fig. 4J). These ridges are

morphologically consistent with networks of interconnected TARs (e.g., Balme et al., 2008). The central pit floor unit forms a ~20–30 m high scarp at its SE margin (Fig. 4J), which suggests that the unit is lithified. This scarp forms the wall of a ~400 m wide trench that separates the central pit floor unit from the SE wall of the central pit. The floor of this trench is occupied by numerous subparallel, trench-transverse TARs

(Fig. 4J).

5.6. Crater wall valleys and upper incised plains

All portions of the wall of Chukhung crater that are not superposed by the LDA or highland mantling units host sinuous, dendritic, kilometer-scale valley networks (Fig. 3 and 4O). These valley networks are considerably smaller than the 100 km-scale, Noachian-aged valley networks in Mars' equatorial regions (e.g., Masursky et al., 1977; Hynek et al., 2010). Many of the crater wall valleys incise smooth deposits (upper incised plains, *Uip*; Figs. 3, 4N, and 11) which occupy topographic lows in the crater wall (e.g. crater wall terraces). In places, they extend several kilometers from the foot of the crater wall to the upslope margins of the upper plains and ridges unit (Fig. 10A). The downslope upper plains and ridges unit overlies the upslope upper incised plains unit (Figs. 5 and 10). In some locations, valleys within the upper incised plains are aligned with sinuous ridges and valleys which extend from the downslope margins of the upper plains and ridges unit (Figs. 3 and 10). Isolated patches of rough, pockmarked material (Isolated pockmarked unit, *Ipo*; Fig. 4H) superpose both the upper incised plains and the upper plains and ridges units (Fig. 10A). The pockmarked texture comprises a mixture of small impact craters and irregular-shaped pits.

5.7. Modeled impact crater retention ages

5.7.1. Estimation of the age of Chukhung crater

Chukhung crater is located within the early-Hesperian volcanic (eHv) unit, defined by Tanaka et al. (2014b) as regionally-sourced flood lavas. Impact crater size-frequency distributions return a best-fit model age of 3.59 Ga for the eHv unit (Tanaka et al., 2014a), providing a maximum bounding age in the early Hesperian period for Chukhung crater.

Fig. 12 shows the size-frequency distribution of impact craters superposed upon the ejecta blanket of the SE rayed crater, which superposes the SE rim of Chukhung crater (Fig. 2). In total, we measured 1457 $D \geq 70$ m impact craters on the superposed impact ejecta (8.63×10^2 km^2; Fig. 2), 1436 of which fall along isochrones defined by Hartmann and Neukum (2001). D (70–150 m) impact craters (n = 1187) follow the 390 ± 10 Ma isochron, D (150 m–350 m) impact craters (n = 239) follow the 780 ± 50 Ma isochron, and D 450 m–700 m) impact craters (n = 10) follow the 2.1 ± 0.6 Ga isochron. We take a cautious approach and use the maximum best-fit estimate of 2.1 ± 0.6 Ga derived from D (450 m–700 m) impact craters as an estimate of the impact crater retention age of the superposed impact ejecta blanket.

Spatial randomness analyses (Fig. 12) of measured impact craters suggest that D (450 m–700 m) craters, from which this age estimate was obtained, are spatially random, and therefore that their size-frequency distribution is unlikely to have been strongly influenced by resurfacing and/or secondary cratering processes. However, this best-fit age is derived from a small sample of impact craters (n = 10) which, combined with the small count area (Warner et al., 2015), introduces significant uncertainty into the 2.1 ± 0.6 Ga age estimate. Spatial randomness analyses show clustering of the D (70 m–350 m) impact craters used to derive fits to the 390 ± 10 Ma and 780 ± 50 Ma isochrons; thus, these fits may reflect resurfacing and/or secondary impact cratering events during the middle Amazonian. Considering these new analyses and the age of
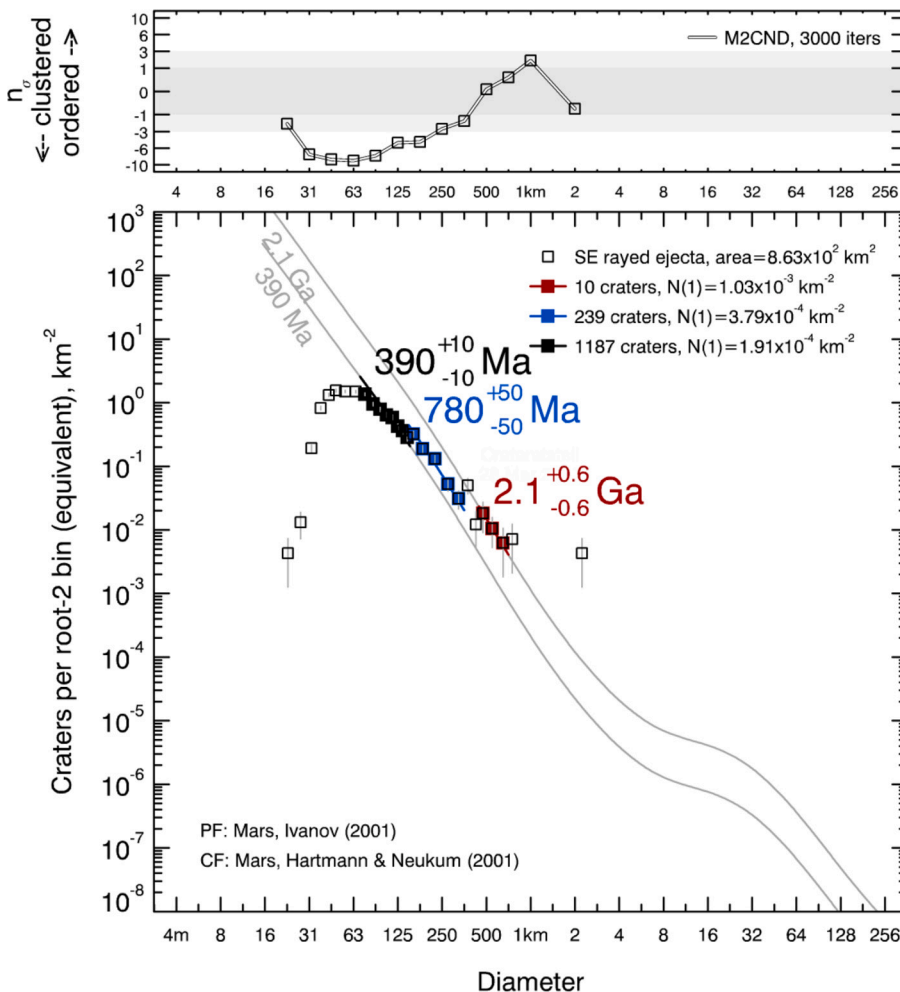

Fig. 12. Impact crater size-frequency distribution for the ejecta blanket of the SE rayed crater. The lower axes are a log incremental plot (Hartmann, 2005) showing best-fit ages that follow three isochrones. Modeled ages are based upon the Ivanov (2001) production function and the Hartmann and Neukum (2001) chronology function. The count area and locations of counted craters are shown in Fig. 2. The roll-off for diameters <70 m represents the lower limit for reliable detection of impact craters. The upper axes show the results of spatial randomness analyses (Michael et al., 2012); the y-axis represents the number of standard deviations by which the M2CND (see text) of 3000 simulated impact crater populations deviates from the M2CND of the real impact crater population. Points within the grey region show that impact craters in the real population for a given diameter bin approximate a spatially random distribution. (For interpretation of the references to color in this figure legend, the reader is referred to the web version of this article.)

the eHv unit within which Chukhung crater is located (Tanaka et al., 2014b), Chukhung crater probably formed ~3.6–2.1 Ga, between the early Hesperian and early Amazonian.

5.7.2. Estimation of the impact crater retention age of VFFs in Chukhung crater

We measured 309 impact craters across all LDAs within Chukhung crater (1.25×10^2 km^2; Fig. 13), 133 of which fall along the Hartmann and Neukum (2001) isochrons. D (50–90 m) impact craters (n = 123) follow the 84 ± 7 Ma isochron, while D (150–300 m) impact craters (n = 10) follow the 330 ± 90 Ma isochron. The majority of D (50–90 m) impact craters on the LDAs have bowl-shaped morphologies, while D (150–300 m) impact craters have 'ring-mold' morphologies which have been attributed to modification of impact craters by deposition and modification of mantling materials comprising ice-dust mixtures atop LDA surfaces (Baker and Carter, 2019). Thus, the best-fit age of 84 ± 7 Ma derived from D (50–90 m) impact craters probably reflects the age of an episode of LDA resurfacing by a mantling deposit during the late Amazonian. The best-fit age of 330 ± 90 Ma derived from D (150–300 m) impact craters probably reflects the minimum age of the LDAs in Chukhung crater, which falls in the mid to late Amazonian.

However, the D (50–200 m) impact craters are not randomly spatially distributed. This could make both modeled best-fit age estimates unreliable. Additionally, dependence upon impact craters with $D < 100$ m was unavoidable, potentially introducing a factor of ten uncertainty in the 84 ± 7 Ma fit (Hartmann, 2005). Unavoidably small count areas mean that the minimum age estimate for LDAs (330 ± 90 Ma) relies upon a small sample of impact craters (n = 10),

introducing additional uncertainty into this estimate (Warner et al., 2015). These uncertainties are unavoidable and necessitate caution in interpretation of the ages of LDAs in Chukhung crater. However, the key result, that the LDAs are young relative to the age of Chukhung crater itself, is robust.

6. Interpretations

The floor of Chukhung crater has undergone significant post-impact modification. We now discuss evidence that post-impact processes within Chukhung crater included subaerial fluvial activity and more recent (possibly wet-based) glaciation. We first summarize the 'esker vs. inverted channel problem' which affects interpretations of the origins of sinuous ridge landforms on Mars (Section 6.1). With this context, we then discuss our hypothesis that the landform assemblage comprising valleys and sinuous ridges in the northern portion of Chukhung crater was formed by non-glacial (i.e., subaerial) fluvial processes, and argue that the northern sinuous ridges are more likely to be inverted paleo-channels than eskers (Section 6.2). We then discuss the hypothesis that landform assemblage comprising the LDA-terminal lobes, ridged plains units, and sinuous ridges in southern Chukhung crater were formed by glaciation, and that the southern sinuous ridges are eskers (Section 6.3). In Section 6.4 we discuss the challenges for distinguishing between esker and inverted paleochannel origins for sinuous ridges and, and in Section 6.5 we explore the alternative hypotheses that all sinuous ridges in Chukhung crater are inverted paleochannels, or that Chukhung crater hosts a mixture of eskers and inverted paleochannels which cannot be divided on a north-south basis. Finally, in Section 7, we discuss the
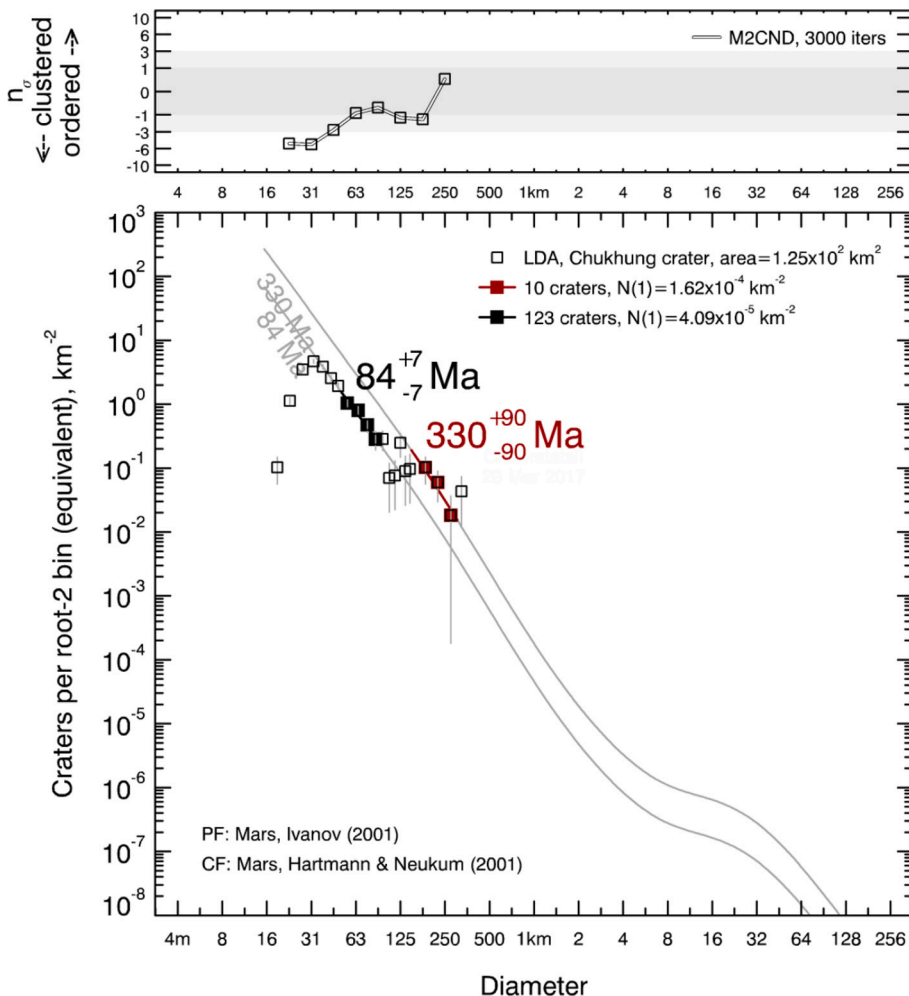

Fig. 13. Impact crater size-frequency distribution for LDAs in Chukhung crater. The lower axes are a log incremental plot (Hartmann, 2005) showing best-fit ages that follow two isochrons. Modeled ages are based upon the Ivanov (2001) production function and the Hartmann and Neukum (2001) chronology function. The roll-off for diameters <50 m represents the lower limit for reliable detection of impact craters. The upper axes show the results of spatial randomness analyses (Michael et al., 2012); the y-axis represents the number of standard deviations by which the M2CND (see text) of 3000 simulated impact crater populations deviates from the M2CND of the real impact crater population. Points within the grey region show that impact craters in the real population for a given diameter bin approximate a spatially random distribution. (For interpretation of the references to color in this figure legend, the reader is referred to the web version of this article.)

paleoenvironmental implications of the landsystem in Chukhung crater.

6.1. The 'esker vs. inverted paleochannel problem'

Previous studies of sinuous ridges on Mars have commonly converged on a debate between their origins as either eskers or inverted paleochannels (e.g., Howard, 1981; Tanaka and Kolb, 2001; Banks et al., 2009; Burr et al., 2009; Williams et al., 2013; Kress and Head, 2015; Butcher et al., 2016). Similarities in the overarching process associated with the formation of eskers and inverted paleochannels (i.e., the exhumation of sedimentary channel fills from bounding material, whether that be ice or sediment) result in convergence of form between eskers and inverted channels.

Confidence in a proposed formation mechanism for a given sinuous ridge on Mars can be enhanced when that sinuous ridge is located within a wider landsystem that is geomorphically consistent with the proposed mechanism (Pain et al., 2007; Burr et al., 2009; Gallagher and Balme, 2015; Butcher et al., 2017). In the cases of the glacier-linked candidate eskers in Phlegra Montes (Gallagher and Balme, 2015) and NW Tempe Terra (Butcher et al., 2017), associations with VFFs and other landforms with possible glacial origins (e.g., moraines) combined with a lack of corroborating contextual evidence for the alternative hypothesis that they are inverted paleochannels, bolsters confidence in their origins as eskers.

An inverted paleochannel origin for sinuous ridges on Mars is often more easily diagnosed than an esker origin. In many locations, topographic inversion not only exhumes individual paleochannels, but paleochannel belts comprising inverted point and scroll bars, and/or cross-cutting channel fills at different stratigraphic levels (Maizels, 1987; Williams et al., 2007; Burr et al., 2009; Cardenas et al., 2018; Hayden et al., 2019; Balme et al., 2020). Such flow migration features have not been identified in association with eskers on Earth; lateral migration of a subglacial conduit typically (though not invariably) causes erosion of deposits that trace former conduit locations. Thus, observations of migration features in association with a sinuous ridge on Mars can improve confidence in an inverted paleochannel origin.

The 'esker vs. inverted paleochannel problem' is most acute in the case of sinuous ridges that are not associated with corroborating evidence for channel migration. Such features may be absent in the vicinity of an inverted paleochannel because of preferential induration and/or preservation of a single channel, or a lack of migration of the original channel (e.g., Williams et al., 2013). Previous workers have appealed to several other geomorphic characteristics to favor either inverted paleochannel or an esker origins for sinuous ridges on Mars, including: (1) ridge crest morphology, (2) relationship of the ridge to the path of steepest topographic descent, (3) 3D ridge morphometry, and (4) ridge sinuosity. However, as we will discuss, there are unresolved caveats for the use of these criteria for distinguishing between eskers and inverted paleochannels on Mars.

6.2. Northern Chukhung crater: fluvial activity and the inverted paleochannel hypothesis

Central pit craters on Mars commonly host valley networks and other landforms of putative fluvial origin (e.g., alluvial fans and paleolake deposits) which have been attributed to localized precipitation and/or snowmelt during the Hesperian or Amazonian (Peel and Fassett, 2013). These valley networks commonly occur on the floors of central pit craters and on the crater walls. In some central pit craters, crater wall valleys are continuous with crater floor valleys. Peel and Fassett (2013) identified Chukhung crater as hosting such valley networks, and noted that several of those valleys are topographically inverted.

Our observations of the northern portion of Chukhung crater are in agreement with those of Peel and Fassett (2013). The ubiquitous occurrence of dendritic valley networks on the unglaciated portions of the walls of Chukhung crater (Fig. 3), and commonly originating near to

the crater rim crest, is consistent with subaerial fluvial drainage from a distributed source, such as rain or snowmelt (Peel and Fassett, 2013). We interpret the upper incised plains unit as fluvial deposits based on the continuity between valleys within this unit and valleys on the crater walls, and the tendency of the unit to occupy topographic lows. The alignment of several valleys within the upper incised plains with finger-like extensions from the downslope margins of the upper plains and ridges unit (Fig. 10) leads us to propose that the upper plains and ridges unit comprises resistant (e.g., indurated and/or coarse-grained) materials. These formed within the upper layer(s) of, or atop, the upper incised plains, and within the crater floor valleys downslope, enabling topographic inversion of channels or channel belts downslope, and the formation of inverted paleochannels.

Combined with the evidence discussed above, the occurrence of many N1-type ridges within negative-relief crater-floor valleys mean that they probably represent inverted valley-interior channels or channel belts (e.g., Cardenas et al., 2018; Davis et al., 2019), and that they were exhumed by removal of more susceptible materials on the valley floors. Sinuous ridges that appear to cross one-another, possibly at different stratigraphic levels, along the major N1-type sinuous ridge network on the NW floor of Chukhung crater (Fig. 11) suggest that the ridges might be remnants of migratory channel systems (e.g., Williams et al., 2007). The rugged texture of the intermediate plains unit in the northern portion of Chukhung crater, and the visual subtlety of the valley walls, suggests that significant regional deflation may have accompanied channel exhumation, but that this deflation was insufficient to completely erase the original host valleys.

The isolated pockmarked unit shows similar relationships with upslope valleys and downslope sinuous ridges to that exhibited by the upper plains and ridges unit (Fig. 4H). However, the limited, discontinuous extent of the isolated pockmarked unit leads us to suggest that it did not have a significant influence on broad-scale topographic inversion of the crater floor. Its pockmarked texture, patchy distribution, and lack of clear source within the crater suggests that it could be an airfall deposit. However, its limited extent makes constraining its origins difficult, so we do not speculate further.

Peel and Fassett (2013) noted common relationships between valley networks and deposits within central pit craters on Mars, which they interpreted as fluvial or lacustrine in origin. Given that some of the northern sinuous ridges grade into the marginal pit floor unit (e.g., Fig. 11), we propose that the marginal pit floor unit could represent erosional remnants of lithified fluvial or lacustrine deposits which were transported to Chukhung crater's central pit by fluvial valley networks. The materials could have been deposited in a paleolake, or they could be highly-eroded remnants of alluvial fan deposits, which may be more consistent with the general slope of the unit towards the SE (Fig. 6). The marginal pit unit probably covered the floor of the central pit more extensively in the past because: (a) there are several isolated mesas of marginal pit floor materials throughout the central pit, including around its N and E margins (Fig. 3); and (b) there is evidence for significant aeolian modification (and possibly removal) of valley-distal materials on the central pit floor (in the central pit floor unit; Fig. 4J). We propose that aeolian-driven retreat of the marginal pit floor unit has exposed the central pit floor unit. Preferential preservation of the marginal pit floor unit close to the termini of the northern sinuous ridges (Figs. 3 and 6) is consistent with the deposition of coarse-grained sediments proximal to the contributory valley networks. Deposition of susceptible, fine-grained sediments in valley-distal positions would explain preferential retreat of the marginal pit floor unit from the central to eastern portions of the central pit. The ~30 m deep trench along the SE margin of the central pit floor (Fig. 4J) unit suggests that post-impact deposits of at least 30 m thickness remain in the central pit floor unit.

Landform relationships on the northern wall and floor of Chukhung crater (including associations of the N1-type sinuous ridges with upslope valleys and possible resistant materials within the upper plains and ridges unit, and evidence for migration of ridge-forming flows) are most

consistent with the origins of the N1 ridges as inverted paleochannels. Combining this with the lack of evidence for past or present glaciation or ice-rich mantling of the northern wall or floor of Chukhung crater, it is considerably more likely that the N1 ridges are inverted paleochannels than that they are eskers. The relationships between sinuous ridges, crater wall valleys, and possible resistant materials in the upper plains and ridges unit, and the migratory characteristics observed for N1-type ridges, are not observed for N2-type ridges. Therefore, some uncertainty remains over the origins of the N2 ridges; however, the alignment of some N2 ridges with the downslope ends of N1 ridges, and the lack of evidence for past or present glaciation on the northern floor of Chukhung crater suggests that they are more likely to be inverted paleochannels than eskers.

6.3. Southern Chukhung crater: glaciation and the esker hypothesis

The southern portion of Chukhung crater is presently glaciated. The convex-up topographic profiles of many portions of the LDAs suggests they may retain substantial cores of debris-covered ice. However, concave topographic profiles in some portions, and the highly tortuous LDA termini (as opposed to smooth, lobate termini) imply that the LDAs have probably undergone significant downwasting and retreat since they reached their maximum volume and extent.

We interpret the LDA-terminal lobes that bound LDAs on the southern floor as moraines formed by downwasting of the LDAs following stagnation of the glacier termini. Hummocks and arcuate ridges within the LDA-terminal lobes are morphologically similar to hummocky moraines on Earth, which commonly contain substantial ice cores (e.g., Hambrey et al., 1997; Krüger and Kjær, 2000). Thus, the LDA-terminal lobes could contain substantial extant ice cores mantled by debris derived from supraglacial dust and/or debris cover. We cannot, however, rule out that some fraction of lithic material in the LDA-terminal lobes was derived from subglacial erosion. In their global survey of martian impact craters using 100–233 m/pixel Thermal Emission Imaging System daytime infrared images, Robbins and Hynek (2012) categorized these features as crater wall slump deposits formed by mass wasting of the crater wall or rim. The higher-resolution CTX and HiRISE images and topographic data analyzed in the present study support a moraine interpretation because: (a) the lobes are consistently spatially associated with LDAs, and (b) we find insufficient evidence for a source region (e.g., consistently spatially-associated crater wall alcoves, depressions in the elevation of the crater rim, or north-south asymmetry of the crater walls) for a slump event of the magnitude implied by the extensive and voluminous nature of the LDA-terminal lobes. Our ice-cored moraine interpretation does not require that the full volume of the LDA-terminal lobes was derived from subglacial erosion of the crater walls/floor. However, we note that the crater wall above the present-day LDA surfaces has a 'planed-off' appearance, which differs from the prominent valley-interfluve morphology of the northern crater wall, and could be related to glacial erosion (Fig. S2). An alternative explanation for the formation of the LDA-terminal lobes is that they are impact ejecta deposits from the SE rayed crater, and we discuss the implications of this hypothesis further below. However, their orientations (particularly of the LDA-terminal lobes in SW and W Chukhung) seem inconsistent with having been sourced from the SE rayed crater. Additionally, their morphologies are different in character to other portions of the ejecta blanket of the SE rayed crater, although it is conceivable that this could result from interaction of impact ejecta with the steep rim topography of Chukhung crater.

The ridged plains unit lacks the decametre-scale undulations observed within the LDA-terminal lobe unit, but its spatial association with other glacigenic units suggests that it could be a ground moraine deposited by the LDAs. However, the ridged plains unit hosts numerous subparallel lineae that align with rays within the ejecta of the SE rayed impact crater located ~10 km SE of Chukhung crater. The northern margin of the ridged plains unit is ~24 km from the NW rim of the SE

rayed crater, which is comparable to the ~25 km distance between its SE rim and the SE margins of its distal ejecta blanket. Thus, the lineations within the ridged plains unit could comprise distal ejecta from that impact (see Section 5.2). The absence of evidence for ejecta or similar lineae on nearby LDAs or LDA-terminal lobes suggests that the ejecta was emplaced prior to the most recent glaciation. Alternatively, the ridged plains unit could have been emplaced as an isolated patch of impact ejecta atop the LDA-terminal lobes, driving deflation of ice within the underlying deposits and explaining the atypical low-relief transition between the LDA-terminal lobe and sinuous ridges via the ridged plains unit in this location. However, the lineae in distal ejecta SE of the parent impact crater (Fig. 14C) are significantly more pristine than the lineae in the ridged plains unit (Fig. 14B) within Chukhung crater, suggesting that the lineae within Chukhung crater have been modified, for example by glacial overprinting. In some locations within the ridged plains unit in Chukhung crater, the lineae are superposed by materials with hummocky morphologies that are similar to (but have lower relief than) those within the LDA-terminal lobes. Thus, the ridged plains unit may comprise distal rayed ejecta from the SE rayed crater, but this impact ejecta may have been modified and partially buried by moraines during subsequent glaciation. The hummocky topography of the LDA-terminal lobe and ridged plains units could have resulted from either sublimation or melting of dead ice. However, we find no evidence of meltwater drainage from the LDA-terminal lobe complex, and therefore argue that sublimation was the dominant or sole contributor to ice loss from this unit.

Given the spatial association of the southern (S1 and S2) sinuous ridges with LDAs (i.e. putative debris-covered glaciers) and possible glacigenic deposits in the LDA-terminal lobe and ridged plains units (Fig. 8), we explore their possible origins as eskers formed during one or more phase(s) of wet-based glaciation in southern Chukhung crater.

Most notable among the esker-like characteristics of the southern sinuous ridges, aside from their associations with glacigenic deposits, are: (a) their ascent of valley walls and topographic divides (e.g., Fig. 8B–D); (b) similarities between their crest morphologies and those of eskers on Earth (e.g., Shreve, 1985; Perkins et al., 2016), being predominantly sharp-crested, but also having round-crested and flat-topped portions (e.g., Fig. 8B–D and 9A–B); and (c) similarities between their typical morphometries and those of martian sinuous ridges for which we are relatively confident of esker origins (Gallagher and Balme, 2015; Butcher et al., 2017; Butcher, 2019; Butcher et al., 2020).

Eskers deposited by pressurized meltwater in ice-confined subglacial conduits commonly ascend topographic undulations due to modification of the direction of steepest hydraulic potential gradient by the overlying ice (e.g., Shreve, 1972, 1985). Thus, subglacial formation as eskers could explain why the S2 sinuous ridges in Chukhung crater do not conform to the axes of the crater floor valleys, and in some cases ascend valley walls and cross onto adjacent plains. In this regard, they are strikingly esker-like (Fig. 15).

Qualitatively, the crest morphologies of both the S1 and S2 ridges are very similar to those of eskers on Earth (e.g., Fig. 15), being dominated by prominent sharp crests. Preliminary measurements suggest that their typical geometries (Section 5.3) are similar to mid-latitude VFF-linked sinuous ridges in Phlegra Montes (Gallagher and Balme, 2015; Butcher, 2019) and NW Tempe Terra (Butcher et al., 2017; Butcher, 2019), for which we are confident of esker origins.

The S1 type sinuous ridges emerge from beneath the LDA-terminal lobe and ridged plains units, which we have interpreted as moraines. Thus, if the southern sinuous ridges are eskers, they pre-date the moraine-forming episode, and the glaciers previously extended beyond the LDA-terminal lobes, up to ~15 km across the crater floor, towards the margins of the central pit. Under the esker hypothesis, one or more episodes of basal melting and esker formation accompanied, or were followed by, glacier retreat. Subsequent glacier stagnation and downwasting of the LDA termini, either by sublimation or melting of ice, could explain the formation of the moraine deposits which superpose the
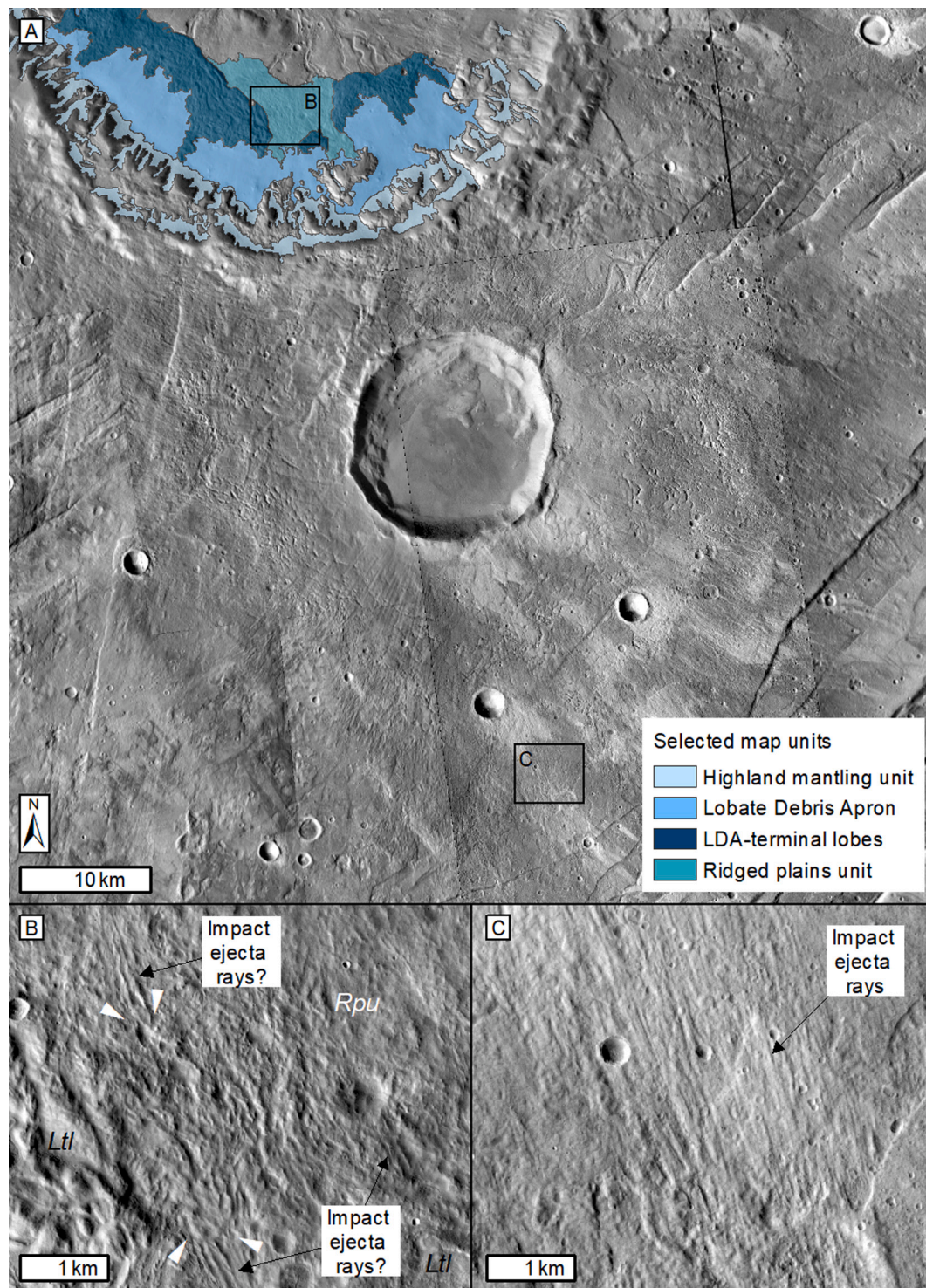
Fig. 14. Evidence for glacial modification of rayed impact ejecta in Chukhung crater. (A) CTX image mosaic (see Table S1) showing the rayed impact crater SE of, and inferred glacial and glacigenic units within, Chukhung crater, and the extents of panels B and C. (B) Possible ejecta from the SE rayed impact crater within the Ridged plains unit (*Rpu*), which appears to have been overprinted (white arrows) by materials that grade into the LDA-terminal lobes (*Ltl*). (C) Rayed ejecta on the opposite (SE) side of the impact ejecta blanket, but at a similar distance from the parent crater rim to panel B. The ejecta rays here are relatively morphologically pristine. This suggests that rayed ejecta within Chukhung crater has been modified by processes that haven't occurred elsewhere on the ejecta blanket (i.e., glaciation). (For interpretation of the references to color in this figure legend, the reader is referred to the web version of this article.)

heads of the sinuous ridges (LDA-terminal lobes and ridged plains units). The absence of moraine ridges at the termini of the sinuous ridges does not pose a significant challenge for the esker hypothesis. Eskers on Earth are commonly found without associated moraines (e.g., Aylsworth and Shilts, 1989), for example due to: transience of wet-based conditions;

short-lived glacial advance followed by continuous retreat; and/or low rates of basal sliding (and hence erosion and sediment production) associated with efficient evacuation of meltwater through esker-forming meltwater conduits.

An esker interpretation of the southern sinuous ridges is dependent
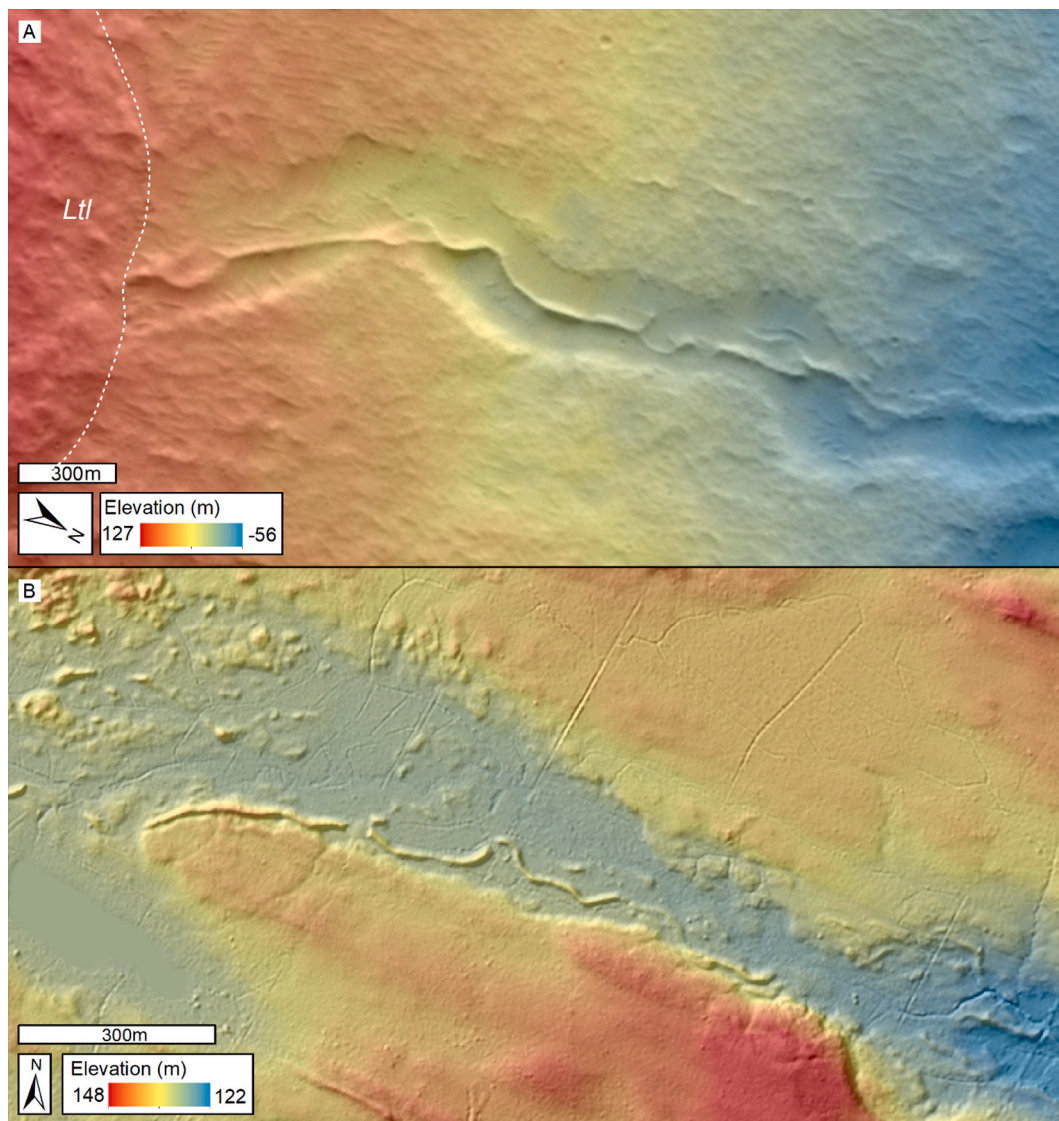
Fig. 15. Similarities in morphology and associations with host valleys between sinuous ridges in Chukhung crater, Mars, and eskers in Finland, Earth. (A) 6 m/pixel CTX image mosaic overlain with 24 m/pixel CTX stereo-pair-derived DEM of an S1-type sinuous ridge which emerges from the LDA-terminal lobe unit and appears to ascend the wall of the crater-floor valley it occupies. Extent shown in Fig. 7. (B) Shaded relief map overlain with 2 m/pixel LiDAR DEM of an esker in southern Finland, Earth (panel centered on 24.117°E, 60.871°N). The esker occupies a broader meltwater valley, and does not adhere to the topography of the valley axis. The similarities in morphology and topographic setting between the ridges in panels A and B are striking. Paleoflow in both panels was from left to right. See Table S1 for list of data products. (For interpretation of the references to color in this figure legend, the reader is referred to the web version of this article.)

upon the interpretation of the LDA-terminal lobes as moraines. If the LDA-terminal lobes are impact ejecta or crater wall-slump deposits (Robbins and Hynek, 2012), these units instead represent a temporal discontinuity between formation of the sinuous ridges that they superpose, and the formation of the LDAs. In this case, units underlying the LDA-terminal lobes, including the sinuous ridges, formed before the SE impact crater ~2.1 Ga. If the ridged plains unit comprises pre-glacial impact ejecta over which glaciers did not subsequently advance, this would also represent a temporal discontinuity between the LDAs upslope and the sinuous ridges downslope. Alternatively, if the ridged plains unit is a patch of outlying impact ejecta emplaced after formation of the LDA-terminal lobes, then the LDAs, LDA-terminal lobes, and sinuous ridges could have formed within the same glacial event. If this scenario is correct, this would suggest that our impact crater size-frequency analyses significantly underestimate the age of the extant glaciers in Chukhung crater, and that the glaciers advanced before the formation of the SE impact crater ~2.1 Ga (i.e., during or prior to the early Amazonian). However, we consider this scenario to be unlikely

based on the apparent superposition of hummocky materials (similar to those within the adjacent LDA-terminal lobes) atop ejecta lineae within the ridged plains unit.

Eskers on Earth are commonly associated with tunnel valleys, which form under erosive regimes of subglacial drainage (e.g., Kehew et al., 2012). If the southern sinuous ridges are eskers, the crater floor valleys with which they are associated could be interpreted as tunnel valleys. However, similar crater floor valleys occur around all portions of Chukhung crater, including in portions with no additional evidence of past or present glaciation. Similar valleys are also common within central pit craters elsewhere on Mars, in which there is often no associated evidence of past or present glaciation (Peel and Fassett, 2013). We find little additional evidence (other than the association of some of the valleys with esker-like sinuous ridges) to challenge the hypothesis of Peel and Fassett (2013) that the crater floor valleys within Chukhung crater are pre-glacial subaerial fluvial valleys of Hesperian or Amazonian age. However, if glaciers within Chukhung crater did subsequently produce meltwater, this meltwater is likely to have exploited pre-

existing valleys. Under the esker hypothesis, this would explain why the southern sinuous ridges generally occupy the valleys; deviations in the paths of the sinuous ridges from the valley axes, and the crossing of S2 ridges out of the valleys, can be explained by localized modification of hydraulic gradients by the overlying ice.

6.4. Challenges for the esker hypothesis

Chukhung crater demonstrates the challenges for interpreting the origins of sinuous ridges on Mars in locations where contextual land-systems consistent with paleochannel inversion (i.e., fluvial valleys, and evidence for channel migration and subsequent landscape deflation) and esker formation (i.e., extant glaciers and glacigenic deposits) coexist in close proximity.

The highland mantling, LDA, LDA-terminal lobe, and ridged plains units obscure topographic lows in the southern crater wall, and the intermediate-to-upper elevations of the southern crater floor. It is in these portions of northern Chukhung crater that the landform associations providing strongest evidence for inverted paleochannel origins of the N1 sinuous ridges (i.e., associations with crater wall valley networks and a possible resistant unit) are observed (Fig. 10). The near-ubiquitous distribution of valley networks on all portions of the crater wall where highland mantling materials are absent suggests that the highland mantling unit could obscure similar valley networks on the southern crater wall. Thus, it is possible that, despite their associations with glacial deposits, the southern sinuous ridges in Chukhung crater are also inverted paleochannels which pre-date glaciation. The SW branch of the major N1-type sinuous ridge network on the NW portion of the crater floor emerges from beneath the LDA-terminal lobe on the SW floor, demonstrating that the LDAs do obscure ridges interpreted as inverted paleochannels in some locations.

In such circumstances where contextual landsystems are consistent with both esker and inverted paleochannel origins for sinuous ridges on Mars, it is necessary to appeal to properties of the ridges themselves to explore possible formation mechanisms. In the sections that follow, we consider the key esker-like characteristics of the southern sinuous ridges in more detail, and highlight the caveats of using some of these characteristics to definitively exclude an inverted paleochannel origin.

6.4.1. Ridge crest morphology

As discussed in Section 5.3, the southern sinuous ridges in Chukhung crater have similar (predominantly sharp-crested) morphologies to eskers on Earth. Arguments that favor esker or inverted paleochannel origins for sinuous ridges based on their typical crest morphologies (e.g., Kargel and Strom, 1992; Pain et al., 2007; Burr et al., 2009) are rooted in an informal understanding that inverted paleochannels are typically flat-topped, and eskers are more often characterized by one or more sharp or rounded medial crests.

However, on Earth, neither morphology is unique to inverted paleochannels or eskers (Fig. 16). Although inverted paleochannels are predominantly flat-topped (Fig. 16A and C; Pain et al., 2007; Williams et al., 2007), they can have crest morphologies (Williams et al., 2013; Chuang and Williams, 2018) that are similar to eskers (Shreve, 1985; Perkins et al., 2016), including: round-crested, sharp-crested, and multi-crested sections, and sections that retain negative-relief troughs (Maizels, 1987; Pain and Oilier, 1995; Williams et al., 2007). Additionally, the crest morphologies of inverted paleochannels can evolve over time. The flat-topped morphology shown in transect C–C′ in Fig. 16A and C results from the preservation of resistant caprock at the crest of an inverted paleochannel on Earth. In the location of transect D–D′ (Fig. 16A and D), however, removal of the caprock has exposed more susceptible underlying materials and subsequent erosion has driven a transition to a sharp-to-round-crested morphology (See also Fig. 10 in Burr et al., 2009). Some eskers on Earth also have flat-topped morphologies (Fig. 16B and F; Kargel and Strom, 1992; Perkins et al., 2016). Flat-topped eskers are thought to form by deposition within subaerial

ice-walled channels, or within subglacial conduits at atmospheric pressure (i.e., under non-channel-full conditions; e.g., Burke et al., 2012; Perkins et al., 2016). Therefore, distinguishing between eskers and inverted paleochannels on Mars based on their crest morphologies alone represents an oversimplification. Indeed, ~40% of the S1 ridges in southern Chukhung crater transition between sharp-crested and flat-topped morphologies at one or more point(s) along their lengths. The predominance of sharp-crested morphologies along the southern sinuous ridges in Chukhung crater, while esker-like, is therefore not uniquely indicative of esker origins, despite striking visual similarities to typical eskers on Earth.

Additionally, N2-type ridges on the northern floor of Chukhung crater (Fig. 9D) have very similar sharp-crested morphologies and scales to many S2-type ridges on the southern floor (Fig. 9B). Some of these N2-type ridges originate close to the downslope ends of N1-type ridges and are aligned with them. There is no evidence for either past or present glaciation of the northern portion of Chukhung crater. Thus, the morphological similarity between N2- and S2-type ridges could be problematic for the esker hypothesis.

6.4.2. Ascent of bedslopes

One of the most commonly-invoked arguments to support esker origins for sinuous ridges on Mars is ascent of bedslopes by those ridges (Head, 2000a, 2000b; Head and Hallet, 2001a, 2001b; Banks et al., 2009; Burr et al., 2009; Butcher et al., 2016, 2017), as we observe for the southern sinuous ridges in Chukhung crater. Under hydraulic pressure within confined subglacial conduits, subglacial meltwater follows the hydraulic gradient, which is controlled primarily by ice surface slope, rather than bed topography (Shreve, 1972, 1985). Thus, esker paths commonly deviate from the steepest topographic slope or even ascend topography. This contrasts markedly with subaerial rivers, whose paths invariably follow the steepest topographic gradient. As a result, ascent of bedslopes (such as we observe for the southern ridges in Chukhung crater) necessarily casts doubt upon inverted paleochannel interpretations for sinuous ridges which ascend topography on Mars.

However, recent studies have demonstrated that the inverted paleochannel hypothesis cannot necessarily be ruled out by observations of bedslope ascent by sinuous ridges (Lefort et al., 2012; Williams et al., 2013). The slopes of inverted paleochannels do not necessarily reflect the original slopes at the beds of ridge-forming flows, owing to spatial variations in induration or armouring, post-exhumation modification (Lefort et al., 2012; Williams et al., 2013), and the fact that inverted paleochannels often comprise composite deposits of migratory flows (e.g., Hayden et al., 2019). Lefort et al. (2012) suggested that apparent slope ascent by inverted paleochannels could result from: (1) differential modification of the channel floor topography before and/or after exhumation, (2) exhumation of multiple generations of paleochannels at different stratigraphic levels, (3) differential erosion of the surrounding region, (4) differential settling and/or compaction of materials underlying the ridge, (5) tectonic deformation, and/or (6) igneous intrusion(s) into the substrate.

Some of the mechanisms identified by Lefort et al. (2012) could, to some extent, explain the ascent of bedslopes by the southern sinuous ridges in Chukhung crater. For example, it is possible that the appearance of a ~ 7 m ascent of a valley wall by the S1 ridge in Fig. 17A–C is an outcome of differential erosion of valley-filling materials surrounding the ridge during exhumation. In the cross-sectional topographic profile of the ridge in Fig. 17E, the base of the eastern flank of the ridge is ~10 m higher in elevation than the western flank. It is possible that material was preferentially eroded from the valley floor to the west of the ridge, and that materials to the east of the ridge have been preferentially preserved. As such, ascent of bedslopes by the S1-type sinuous ridge in Fig. 17 is not necessarily uniquely indicative of an esker origin.

The sharp-crested S2-type sinuous ridges that superpose the flat-topped S1-type sinuous ridges in Fig. 9E could represent locations where differential erosion and/or compaction of inverted paleochannels
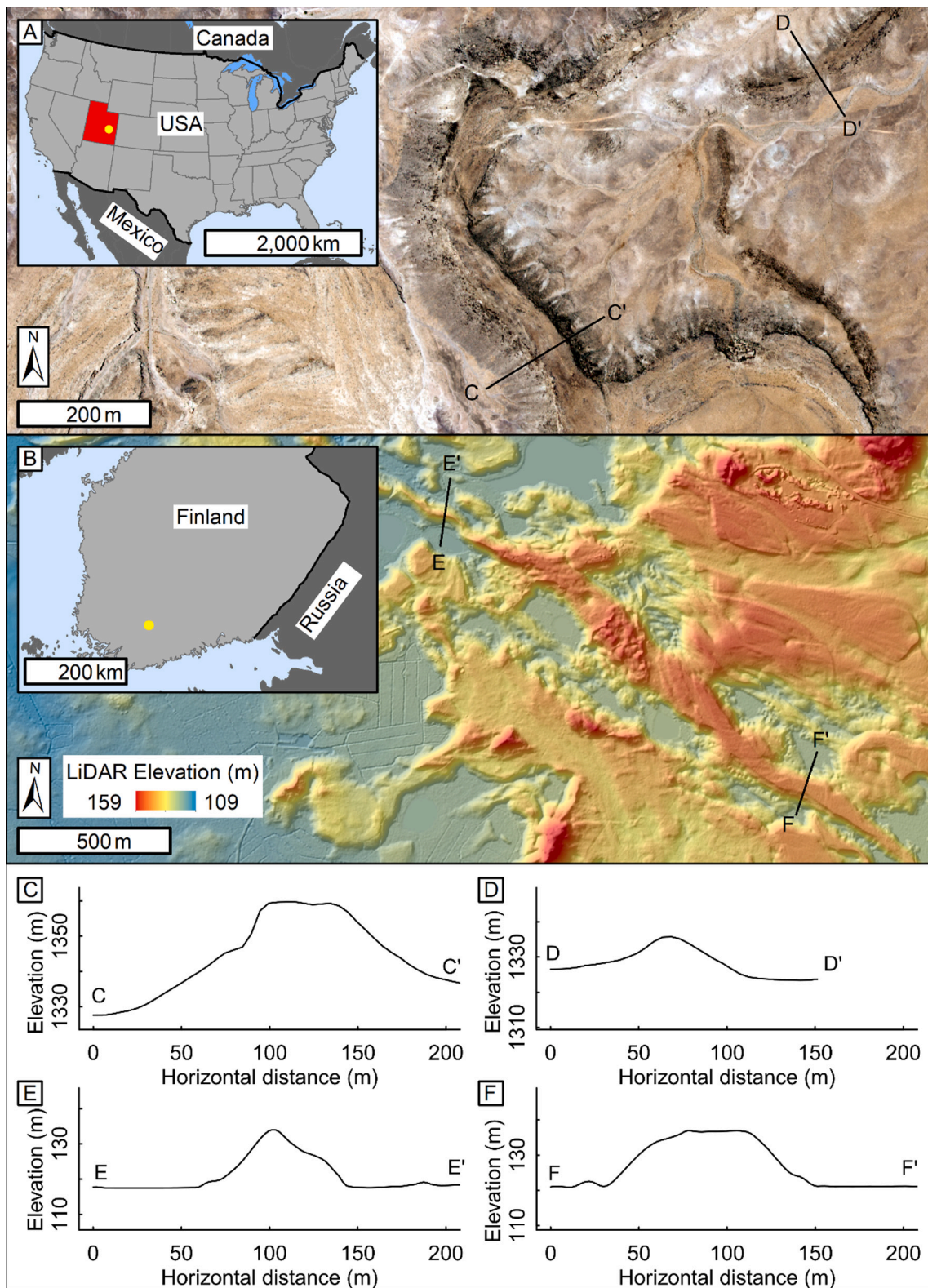
Fig. 16. Morphological similarities between eskers and inverted paleochannels on Earth. (A) Aerial orthophotograph (illumination from left) of inverted paleo-channels in Utah (location 110.273°W, 38.878°N shown by yellow point in inset map) showing locations of cross-sectional topographic profiles (at 5 m/pixel resolution) C–C′ (panel C, a flat-topped portion), and D–D′ (panel D, a sharp- to round-crested portion). (B) 2 m/pixel LiDAR DEM of an esker in SW Finland (location 23.992°E, 60.746°N shown by yellow point in inset map) showing locations of cross-sectional topographic profiles E–E′ (panel E, a sharp-crested portion), and F–F′ (panel F, a flat-topped portion). See Table S1 for data products. (For interpretation of the references to colour in this figure legend, the reader is referred to the web version of this article.)
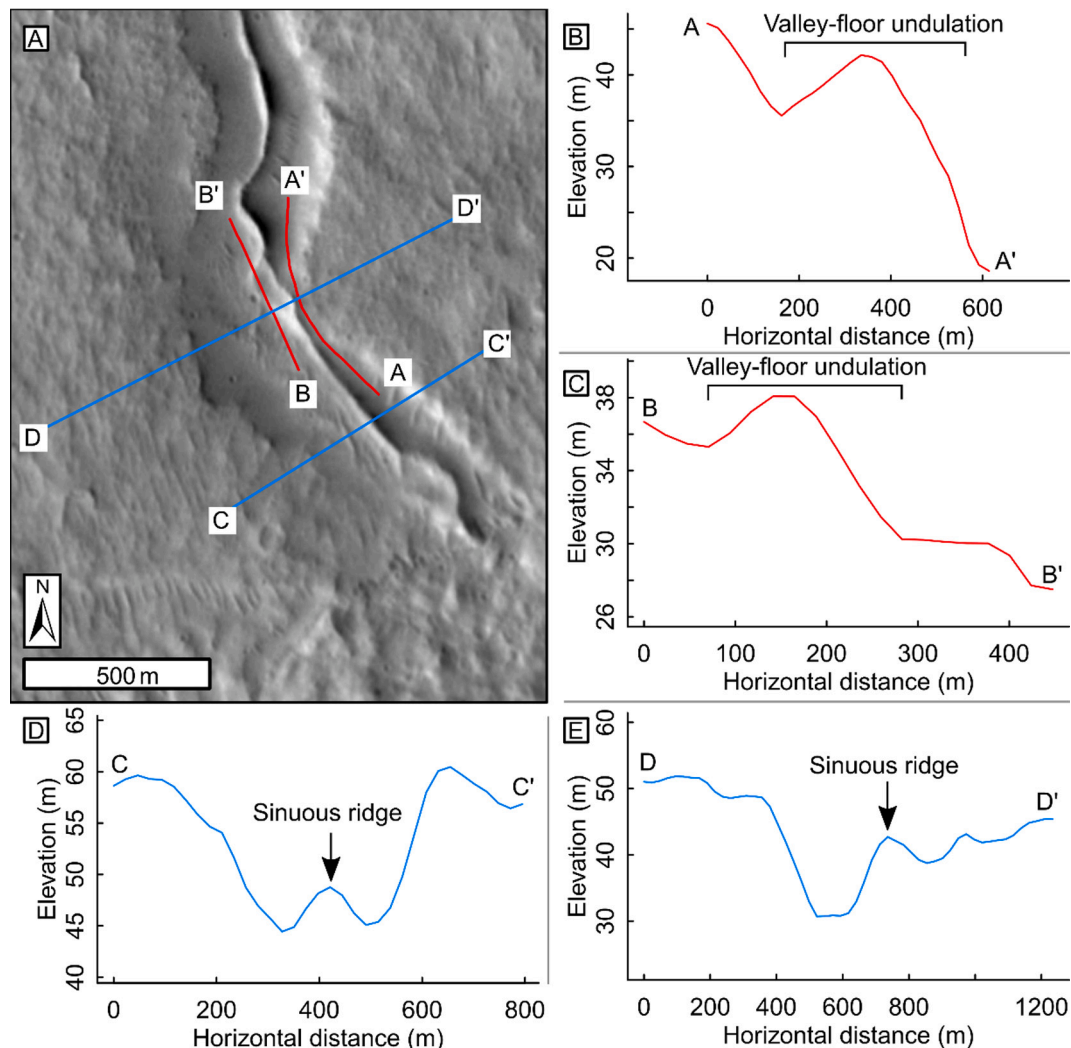
Fig. 17. The possible role of differential erosion in the ascent of present-day bedslopes by sinuous ridges in Chukhung crater. (A) CTX image of an S1-type sinuous ridge in southern Chukhung crater (location in Fig. 7). It appears to ascend ~7 m up the wall of the valley it occupies. Colored lines show locations of topographic profiles (obtained from the CTX DEM; Table S1) in panels B–E. (B) Topographic profile A–A′ showing the ~7 m along-ridge undulation in the present-day topography of the valley to the east of the sinuous ridge. (C) Topographic profile B–B′ showing the along-ridge undulation in the present-day topography of the valley to the west of the sinuous ridge. (D) Valley-transverse topographic profile C–C′ showing the sinuous ridge where it occupies the bottom of the valley floor. (E) Valley-transverse topographic profile D–D′ showing the sinuous ridge where it appears to be 'perched' part way up the valley floor. It should be noted that the width of the sinuous ridge approaches the 24 m/pixel horizontal resolution of the CTX DEM available for this location. See Table S1 for data products. (For interpretation of the references to color in this figure legend, the reader is referred to the web version of this article.)

at different stratigraphic levels gives the impression that flows forming stratigraphically-higher ridges ascended paleo-bedslopes.

Under the slope-modification mechanisms outlined by Lefort et al. (2012) it is, however, harder to explain the observation that S2 ridges occasionally exit the valley sides and cross onto the adjacent plains. The deposits comprising the S2 ridges could have formed at the elevation of the valley-adjacent plains at a time when the underlying valleys were buried, and could have subsequently been lowered into the valleys by preferential compaction of valley-filling materials. However, in some locations where S2 ridges cross over the valley sides, the portions of the ridges occupying the valley floors are significantly smaller in scale (typically <5 m high) than the relief of the valley walls (~25–30 m) they ascend. Thus compaction of materials beneath the portions of the S2 ridges that occupy the valley floors would require the emplacement and subsequent removal of a significant thickness of material atop the ridges. We find no evidence for such burial and subsequent exhumation. We consider the crossing of the S2 ridges out of valleys and on to valley-adjacent plains to provide the most robust evidence for esker origins of these ridges.

6.4.3. 3D morphometry

The southern sinuous ridges in Chukhung crater have typical heights and widths that are comparable to those of VFF-linked sinuous ridges in Phlegra Montes and NW Tempe Terra (Butcher, 2019; Butcher et al., 2020). This suggests that they could share a common formation mechanism. However, the southern sinuous ridges (particularly the S2 type ridges) appear to be morphometrically similar to the N2 type ridges on the northern floor. Additionally, there is limited existing knowledge of the morphometries of inverted paleochannels on Earth, or of sinuous ridges on Mars for which there is general consensus for inverted paleochannel origins. The same is true for eskers; no systematic survey of the 3D morphometries of a large sample of eskers on Earth has yet been completed. Thus, it is not yet known whether inverted paleochannels and eskers on either Earth or Mars have distinct morphometric signatures which can be used to diagnose an esker origin. Our ongoing systematic morphometric analyses of sinuous ridges in Chukhung crater and elsewhere on both Mars (e.g., Butcher et al., 2020) and Earth, will provide better insight into the morphometric signatures of sinuous ridges in Chukhung crater and elsewhere on Mars and Earth.

6.4.4. Sinuosity

Several workers have invoked differences between the typical sinuosities of eskers and rivers on Earth to distinguish between esker and inverted paleochannel origins for sinuous ridges on Mars (Metzger, 1992; Kargel, 1993; Banks et al., 2009; Burr et al., 2009; Williams et al., 2013; Kress and Head, 2015; Butcher et al., 2016). Eskers in Canada typically have low sinuosities, with median values <1.1 (Storrar et al., 2014), while meandering rivers typically have sinuosities >1.3 (Schumm, 1963). In this regard, some of the S2 sinuous ridges are somewhat atypical of eskers on Earth, having sinuosities up to ~1.6, while the S1 sinuous ridges have sinuosities that are more similar to eskers on Earth, with values up to ~1.2.

However, specific sinuosity ranges are not unique to either eskers or inverted paleochannels on Earth. For example, eskers in Canada (Storrar et al., 2014) have sinuosities ranging up to 2.62 (i.e. higher than the sinuosity of the S2 ridges), albeit very rarely. High (i.e. >1.3) sinuosities are most common, though still unusual, among the Canadian eskers with length scales similar to those in Chukhung crater (a few kilometers; Storrar et al., 2014). Similarly, many subaerial rivers have sinuosities lower than 1.3; indeed, four of the five inverted paleochannels measured by Maizels (1987) in Oman had sinuosities <1.1, similar to typical sinuosity values recorded by Storrar et al. (2014) for eskers in Canada. Thus, sinuosity cannot necessarily be used to reliably distinguish between eskers and inverted paleochannels.

6.5. Proposed origins of sinuous ridges in Chukhung crater

We are confident that the N1-type sinuous ridges in Chukhung crater are inverted paleochannels based on their associations with valleys on the crater walls and within the upper incised plains unit (e.g., Fig. 10), relationships to possible resistant materials in the upper plains and ridges unit, evidence for flow migration (Fig. 11) and extensive subsequent landscape deflation, and a lack of evidence for either past or present glaciation on the northern walls or floor of Chukhung crater. The alignment of some N2 ridges with the downslope ends of some N1 type ridges, and their lack of spatial association with units of inferred glacial origin suggests that they are also more likely to be inverted paleochannels. However, the interpretation of the N2 ridges as inverted paleochannels is less certain than that for the N1 ridges.

The origins of the southern sinuous ridges are ambiguous; there is evidence to support both esker and inverted paleochannel origins. They are associated with (and commonly emerge from) glacigenic deposits including extant VFFs (putative debris-covered glaciers) and moraine-like units, and have numerous esker-like characteristics. However, many of these characteristics could also be explained under the inverted paleochannel hypothesis. The associations between the S1 ridges and non-glacial units in the southern Chukhung crater are similar to those of the N1 (i.e. inverted paleochannel-like) ridges, such that it is possible that both the N1 and S1 ridges are inverted paleochannels. Importantly, however, the relationships of the S2 ridges to non-glacial units (i.e. the fact that the S2 ridges commonly ascend valley walls and cross onto valley-adjacent plateaus) is harder to explain under the inverted paleochannel hypothesis. Thus, among the sinuous ridges in Chukhung crater, S2 ridges are the strongest candidates as eskers. Notable morphologic similarities between N2 and S2 ridges means that we also do not rule out esker origins for the N2 ridges.

Given our confidence that the N1 sinuous ridges are inverted paleochannels, it is very unlikely that all sinuous ridges in Chukhung crater are eskers. Based on the balance of evidence presented here, we consider the most probable scenarios to be either that: (Scenario 1), the N1, N2, and S1 ridges are inverted paleochannels, and the S2 ridges are eskers; or (Scenario 2), that the northern sinuous ridges are inverted paleochannels, and the southern sinuous ridges are eskers. Other possible scenarios that we consider to be less likely, but which warrant further investigation, include: (Scenario 3) that all sinuous ridges in Chukhung crater are inverted paleochannels; (Scenario 4), that the N1 ridges are

inverted paleochannels, and the N2, S1, and S2 ridges are eskers; and (Scenario 5), that the N1 and S1 ridges are inverted paleochannels, and that the N2 and S2 ridges are eskers. Ongoing detailed morphometric analyses of sinuous ridges in Chukhung crater, and comparisons to analogous landforms on both Earth and Mars aim to test Scenarios 1–5 further. Scenario 3 would require additional explanation for how sinuous ridges could cross out of their host valleys under the inverted paleochannel hypothesis, while scenarios 4 and 5 would require an explanation for the apparent asymmetry in the preservation of glacigenic deposits between the northern and southern portions of Chukhung crater.

7. Paleoenvironmental implications

Regardless of which of the scenarios outlined in Section 6.5 is true, sinuous ridges in Chukhung crater represent protracted and/or episodic periods of wet conditions (subaerially, and possibly also subglacially) between the early Hesperian and mid Amazonian (~3.6–2.1 Ga; Section 5.7). Chukhung crater is one of a growing number of case studies demonstrating the occurrence of post-Noachian fluvial activity within impact craters on Mars (e.g., Grant and Wilson, 2011; Mangold et al., 2012; Kite et al., 2017; Vijayan et al., 2020).

Multi-stage subaerial fluvial drainage which formed the N1 ridges (including features suggestive of channel migration; Fig. 11) in Chukhung crater is consistent with the interpretations of Peel and Fassett (2013), that many central pit craters on Mars probably experienced protracted fluvial activity during the Hesperian or Amazonian. The ~3.6–2.1 Ga age envelope that we have modeled for Chukhung crater is consistent with the observations of Peel and Fassett (2013), and with the occurrence of fluvial activity in Chukhung crater after the period of major valley network formation on Mars (e.g., Fassett and Head, 2008; Hynek et al., 2010).

Under scenarios 1, 2, and 3 outlined in Section 6.5, notable differences in sinuosity between ridge populations interpreted as inverted paleochannels could suggest that hydraulic conditions of subaerial drainage in Chukhung crater varied through time. Maizels (1987) invoked increased grain size of entrained sediments, and increases in peak flow depths and velocities to explain the decrease in sinuosity between stratigraphically-lower (i.e. older, with sinuosities of >1.7) and stratigraphically-higher (i.e., younger, with sinuosities of ~1.03) inverted paleochannels in Oman. The increase in typical sinuosities between older (e.g., N1 and S1) and younger (e.g., S2 and N2) sinuous ridges in Chukhung crater is of similar magnitude but the opposite sense (i.e., an increase in sinuosity towards stratigraphically-higher ridges) to that observed by Maizels (1987). If the ridges are inverted paleochannels, this could be explained by reductions in sediment grain size, flow depths, and velocities towards later subaerial drainage events. Factors that could have promoted such transitions include: reductions in the slope of the crater wall and floor due to relaxation and/or infilling of crater topography, reductions in sediment supply and/or flow power under drying climate conditions, or alternatively an increase in hydraulic base level (e.g., the flow depth of a possible lake in the central pit) under wetter climate conditions.

If any of the sinuous ridges in Chukhung crater are eskers, the location of the crater within an extensive tectonic rift system is consistent with the growing body of evidence (Gallagher and Balme, 2015; Butcher et al., 2017; Arnold et al., 2019; Sori and Bramson, 2019) that elevated geothermal heat flux was a pre-requisite for recent wet-based glaciation on Mars. Considering the uncertainties discussed in Section 5.7.2, the best-fit model age obtained for LDAs in Chukhung crater (330 ± 90 Ma) suggests that the LDA formation, and therefore a possible esker-forming melt episode, could have occurred at a broadly similar time to esker-forming melt episodes in glaciated tectonic rifts/graben in NW Tempe Terra (~110 ± 10 Ma; Butcher et al., 2017) and Phlegra Montes (~150 ± 20 Ma; Gallagher and Balme, 2015). Although the Tempe Fossae rift system and associated volcanic constructs are thought

to have ceased major activity during the late Hesperian (Hauber and Kronberg, 2001; Hauber et al., 2010), we cannot exclude the possibility of late-stage subsurface activity associated with this system continued into the Amazonian. Further investigation of the tectonic and volcanic history of the wider region could aid understanding of possible geothermal influences upon mid- to late-Amazonian glacial melting in Chukhung crater. It should be noted that numerical modeling experiments suggest that for basal melting to have occurred during the Amazonian period, geothermal heating would need to be supplemented by other drivers such as viscous strain heating within glacial ice, small-magnitude climate warming, and/or melting point depression by salts (Butcher et al., 2017; Sori and Bramson, 2019). Mid-latitude climate fluctuations during the Amazonian (see Fig. 7 in Haberle et al., 2003) were probably insufficient to have operated alone in inducing basal melting of glacial ice deposits.

Finally, if the N2 sinuous ridges are eskers (Scenarios 4 and 5 in Section 6.5, which we consider to be the least likely of Scenarios 1–5), or our interpretation of the LDA-terminal lobes as moraines is incorrect (our leading alternative hypothesis being that they are impact ejecta), candidate eskers in Chukhung crater could be the product of an earlier glaciation predating the extant LDAs and LDA-terminal lobes in Chukhung crater. If the LDA-terminal lobes are impact ejecta from the SE rayed crater, our best-fit model age for the SE rayed crater would provide a minimum bounding age of 2.1 Ga for esker formation in Chukhung crater. However, our analyses suggest that the LDA-terminal lobes are more likely to be moraines than impact ejecta, and that the N2 ridges are more likely to be inverted paleochannels than eskers.

8. Conclusions

Chukhung crater, Mars, has undergone complex geologic evolution since its formation between the early Hesperian and early Amazonian periods. Its interior has been modified by subaerial (and possibly subglacial) flows of liquid water, glaciation, and extensive landscape erosion. Sinuous ridges in northern Chukhung crater are best explained as inverted paleochannels comprising exhumed fluvial sediments deposited by subaerial flows of water draining from the northern crater wall. Sinuous ridges in southern Chukhung crater emerge from the terminal deposits of extant debris-covered glaciers. Esker-like characteristics of S1-type sinuous ridges, which occupy crater-floor valleys, could be explained under either the esker or inverted paleochannel hypothesis, hence we are uncertain about their origins. S2-type sinuous ridges in southern Chukhung crater are the strongest esker candidates in Chukhung crater; existing explanations for the apparent ascent of topography by inverted paleochannels cannot adequately explain the fact that the S2 sinuous ridges commonly ascend relatively high-relief walls of crater-floor valleys and cross onto valley-adjacent plains. To summarize we are confident that the N1 sinuous ridges are inverted paleochannels, and consider it most likely that the N2 sinuous ridges are also inverted paleochannels. The inverted paleochannel and esker hypotheses provide similarly strong explanations for the S1-type sinuous ridges, but we find that the esker hypothesis provides a better explanation for the properties of the S2 sinuous ridges.

Chukhung crater provides a valuable case study highlighting several challenges that remain for the identification of eskers on Mars. Esker identification is complicated by similarities in form between eskers and inverted paleochannels. Confidence that a sinuous ridge on Mars is an esker can be significantly improved if that sinuous ridge is associated with extant ice deposits such as VFFs, and there is no associated evidence for deflation or topographic inversion of the surrounding landscape. However, in locations such as Chukhung crater, landsystems that are consistent with both esker and inverted paleochannel origins coexist in close proximity. This complicates definitive interpretation of VFF-linked sinuous ridges as eskers and explains, in particular, our caution over the interpretation of the S1 ridges (which emerge from beneath glacigenic deposits and appear esker-like, but have no apparent

characteristics that cannot also be explained under the inverted paleochannel hypothesis).

Sinuous ridges interpreted as inverted paleochannels in northern and possibly also southern Chukhung crater provide evidence for multiple prolonged episodes of distributed, possibly precipitation- or snowmelt-driven, subaerial fluvial activity and sedimentary aggradation between the early Hesperian and mid Amazonian (Peel and Fassett, 2013). Thus, Chukhung crater or the wider central Tempe Terra region probably experienced climate conditions that were unusually warm and wet compared to the generally cold and dry climate conditions that are thought to have prevailed during that time period.

If the southern sinuous ridges (S2-type and possibly also S1-type) in Chukhung crater are eskers formed by basal melting of mid- to late-Amazonian-aged glaciers in Chukhung crater, their location in a tectonic rift zone is consistent with the possible influence of geothermal heating upon basal melting of their parent glaciers. However, further analyses of the regional tectono-magmatic history are required to assess the likelihood that elevated geothermal heat flux persisted into the period following glacial advance within Chukhung crater.

Supplementary data to this article can be found online at https://doi.org/10.1016/j.icarus.2020.114131.

References

Arnold, N.S., Conway, S.J., Butcher, F.E.G., Balme, M.R., 2019. Modeled subglacial water flow routing supports localized intrusive heating as a possible cause of basal melting of Mars' south polar ice cap. J. Geophys. Res. Planets 124, 2101–2116. https://doi.org/10.1029/2019JE006061.

Aylsworth, J.M., Shilts, W.W., 1989. Glacial Features around the Keewatin Ice Divide: Districts of Mackenzie and Keewatin. Geological Survey of Canada. Map 24-1987, Scale 1:1,000,000.

Baker, D.M.H., Carter, L.M., 2019. Probing supraglacial debris on Mars 2: crater morphology. Icarus 319, 264–280. https://doi.org/10.1016/j.icarus.2018.09.009.

Balme, M., Berman, D.C., Bourke, M.C., Zimbelman, J.R., 2008. Transverse aeolian ridges (TARs) on Mars. Geomorphology 101, 703–720. https://doi.org/10.1016/j.geomorph.2008.03.011.

Balme, M.R., Gupta, S., Davis, J.M., Fawdon, P., Grindrod, P.M., Bridges, J.C., Sefton-Nash, E., Williams, R.M.E., 2020. Aram dorsum: an extensive mid-noachian age fluvial depositional system in Arabia Terra, Mars. J. Geophys. Res. Planets 125, e2019JE006244,. https://doi.org/10.1029/2019JE006244.

Banks, M.E., Lang, N.P., Kargel, J.S., McEwen, A.S., Baker, V.R., Grant, J.A., Pelletier, J.D., Strom, R.G., 2009. An analysis of sinuous ridges in the southern Argyre Planitia, Mars using HiRISE and CTX images and MOLA data. J. Geophys. Res. 114, E09003 https://doi.org/10.1029/2008JE003244.

Burke, M.J., Brennand, T.A., Perkins, A.J., 2012. Transient subglacial hydrology of a thin ice sheet: insights from the Chasm esker, British Columbia, Canada. Quat. Sci. Rev. 58, 30–55. https://doi.org/10.1016/j.quascirev.2012.09.004.

Burr, D.M., Enga, M.-T., Williams, R.M.E., Zimbelman, J.R., Howard, A.D., Brennand, T. A., 2009. Pervasive aqueous paleoflow features in the Aeolis/Zephyria Plana region, Mars. Icarus 200, 52–76. https://doi.org/10.1016/j.icarus.2008.10.014.

Butcher, F.E.G., 2019. Wet-Based Glaciation on Mars (PhD Thesis). The Open University, Milton Keynes, UK. http://oro.open.ac.uk/id/eprint/60703.

Butcher, F.E.G., Conway, S.J., Arnold, N.S., 2016. Are the Dorsa Argentea on Mars eskers? Icarus 275, 65–84. https://doi.org/10.1016/j.icarus.2016.03.028.

Butcher, F.E.G., Balme, M.R., Gallagher, C., Arnold, N.S., Conway, S.J., Hagermann, A., Lewis, S.R., 2017. Recent basal melting of a mid-latitude glacier on Mars. J. Geophys. Res. Planets 122, 2445–2468. https://doi.org/10.1002/2017JE005434.

Butcher, F.E.G., Balme, M.R., Conway, S.J., Gallagher, C., Arnold, N.S., Storrar, R.D., Lewis, S.R., Hagermann, A., 2020. Morphometry of a glacier-linked esker in NW Tempe Terra, Mars, and implications for sediment-discharge dynamics of subglacial drainage. Earth Planet. Sci. Lett. 542, 116325. https://doi.org/10.1016/j.epsl.2020.116325.

Cardenas, B.T., Mohrig, D., Goudge, T.A., 2018. Fluvial stratigraphy of valley fills at Aeolis Dorsa, Mars: evidence for base-level fluctuations controlled by a downstream water body. GSA Bull. 130, 484–498. https://doi.org/10.1130/B31567.1.

Christensen, P.R., Jakosky, B.M., Kieffer, H.H., Malin, M.C., McSween Jr., H.Y., Nealson, K., Mehall, G.L., Silverman, S.H., Ferry, S., Caplinger, M., Ravine, M., 2004. The Thermal Emission Imaging System (THEMIS) for the Mars 2001 Odyssey Mission. Space Sci. Rev. 110, 85–130. https://doi.org/10.1023/B:SPAC.0000021008.16305.94.

Chuang, F.C., Williams, R.M.E., 2018. Valley network morphology in the greater Meridiani Planum region, Mars. J. Maps 14, 652–660. https://doi.org/10.1080/17445647.2018.1530154.

Davis, J.M., Gupta, S., Balme, M., Grindrod, P.M., Fawdon, P., Dickeson, Z.I., Williams, R.M.E., 2019. A diverse array of fluvial depositional systems in Arabia Terra: evidence for mid-Noachian to early Hesperian rivers on Mars. J. Geophys. Res. Planets 124, 1913–1934. https://doi.org/10.1029/2019JE005976.

Edwards, C.S., Nowicki, K.J., Christensen, P.R., Hill, J., Gorelick, N., Murray, K., 2011. Mosaicking of global planetary image datasets: 1. Techniques and data processing for Thermal Emission Imaging System (THEMIS) multi-spectral data. J. Geophys. Res. 116 https://doi.org/10.1029/2010JE003755. E10008.

Fassett, C.I., Head, J.W., 2008. The timing of martian valley network activity: constraints from buffered crater counting. Icarus 195, 61–89. https://doi.org/10.1016/j.icarus.2007.12.009.

Gallagher, C., Balme, M., 2015. Eskers in a complete, wet-based glacial system in the Phlegra Montes region, Mars. Earth Planet. Sci. Lett. 431, 96–109. https://doi.org/10.1016/j.epsl.2015.09.023.

Grant, J.A., Wilson, S.A., 2011. Late alluvial fan formation in southern Margaritifer Terra, Mars. Geophys. Res. Lett. 38 https://doi.org/10.1029/2011GL046844.

Haberle, R.M., Murphy, J.R., Schaeffer, J., 2003. Orbital change experiments with a Mars general circulation model. Icarus 161, 66–89. https://doi.org/10.1016/S0019-1035(02)00017-9.

Hambrey, M.J., Huddart, D., Bennett, M.R., Glasser, N.F., 1997. Genesis of 'hummocky moraines' by thrusting in glacier ice: evidence from Svalbard and Britain. J. Geol. Soc. 154, 623–632. https://doi.org/10.1144/gsjgs.154.4.0623.

Hartmann, W.K., 2005. Martian cratering 8: Isochron refinement and the chronology of Mars. Icarus 174, 294–320. https://doi.org/10.1016/j.icarus.2004.11.023.

Hartmann, W.K., Neukum, G., 2001. Cratering chronology and the evolution of Mars. Space Sci. Rev. 96, 165–194. https://doi.org/10.1023/A:1011945222010.

Hauber, E., Kronberg, P., 2001. Tempe fossae, Mars: a planetary analogon to a terrestrial continental rift? J. Geophys. Res. 106, 20587–20602. https://doi.org/10.1029/2000JE001346.

Hauber, E., Grott, M., Kronberg, P., 2010. Martian rifts: structural geology and geophysics. Earth Planet. Sci. Lett. 294, 393–410. https://doi.org/10.1016/j.epsl.2009.11.005.

Hayden, A.T., Lamb, M.P., Fischer, W.W., Ewing, R.C., McElroy, B.J., Williams, R.M.E., 2019. Formation of sinuous ridges by inversion of river-channel belts in Utah, USA, with implications for Mars. Icarus 332, 92–110. https://doi.org/10.1016/j.icarus.2019.04.019.

Head, J.W., 2000a. Tests for Ancient Polar Deposits on Mars: Origin of Esker-Like Sinuous Ridges (Dorsa Argentea) Using MOLA Data. Lunar and Planetary Science Conference XXXI. Abstract #1116.

Head, J.W., 2000b. Tests for Ancient Polar Deposits on Mars: Morphology and Topographic Relationships of Esker-Like Sinuous Ridges (Dorsa Argentea) Using MOLA Data. Lunar and Planetary Science Conference XXXI. Abstract #1117.

Head, J.W., Hallet, B., 2001a. Origin of Sinuous Ridges in the Dorsa Argentea Formation: New Observations and Tests of the Esker Hypothesis. Lunar and Planetary Science Conference XXXII. Abstract #1373.

Head, J.W., Hallet, B., 2001b. Origin of Sinuous Ridges in the Dorsa Argentea Formation: Additional Criteria for Tests of the Esker Hypothesis. Lunar and Planetary Science Conference XXXII. Abstract #1366.

Head, J.W., Marchant, D.R., Dickson, J.L., Kress, A.M., Baker, D.M., 2010. Northern mid-latitude glaciation in the late Amazonian period of Mars: criteria for the recognition of debris-covered glacier and valley glacier landsystem deposits. Earth Planet. Sci. Lett. 294, 306–320. https://doi.org/10.1016/j.epsl.2009.06.041.

Holt, J.W., Safaeinili, A., Plaut, J.J., Head, J.W., Phillips, R.J., Seu, R., Kempf, S.D., Choudhary, P., Young, D.A., Putzig, N.E., Biccari, D., Gim, Y., 2008. Radar sounding evidence for buried glaciers in the southern mid-latitudes of Mars. Science 322, 1235–1238. https://doi.org/10.1126/science.1164246.

Howard, A.D., 1981. Etched plains and braided ridges of the south polar region of mars: features produced by basal melting of ground ice?. In: Reports of Planetary Geology Program 1981: National Aeronautics and Space Administration Technical Memorandum 84211, pp. 286–288.

Hynek, B.M., Beach, M., Hoke, M.R.T., 2010. Updated global map of Martian valley networks and implications for climate and hydrologic processes. J. Geophys. Res. 115, E09008 https://doi.org/10.1029/2009JE003548.

Ivanov, B.A., 2001. Mars/Moon cratering rate ratio estimates. Space Sci. Rev. 96, 87–104. https://doi.org/10.1023/A:1011941121102.

Jaumann, R., Neukum, G., Behnke, T., Duxbury, T.C., Eichentopf, K., Flohrer, J., Gasselt, S.v., Giese, B., Gwinner, K., Hauber, E., Hoffmann, H., Hoffmeister, A., Köhler, U., Matz, K.-D., McCord, T.B., Mertens, V., Oberst, J., Pischel, R., Reiss, D., Ress, E., Roatsch, T., Saiger, P., Scholten, F., Schwarz, G., Stephan, K., Wählisch, M., 2007. The high-resolution stereo camera (HRSC) experiment on Mars Express: instrument aspects and experiment conduct from interplanetary cruise through the nominal mission. Planet. Space Sci. 55, 928–952. https://doi.org/10.1016/j.pss.2006.12.003.

Kargel, J.S., 1993. Geomorphic processes in the Argyre-Dorsa Argentea region of Mars. Lunar and Planetary Science Conference XXIV. Abstract #1378.

Kargel, J.S., Strom, R.G., 1992. Ancient glaciation on Mars. Geology 20, 3–7. https://doi.org/10.1130/0091-7613(1992)020<0003:AGOM>2.3.CO;2.

Kehew, A.E., Piotrowski, J.A., Jørgensen, F., 2012. Tunnel valleys: concepts and controversies — a review. Earth Sci. Rev. 113, 33–58. https://doi.org/10.1016/j.earscirev.2012.02.002.

Kite, E.S., Sneed, J., Mayer, D.P., Wilson, S.A., 2017. Persistent or repeated surface habitability on Mars during the late Hesperian – Amazonian. Geophys. Res. Lett. 44, 3991–3999. https://doi.org/10.1002/2017GL072660.

Kneissl, T., van Gasselt, S., Neukum, G., 2011. Map-projection-independent crater size-frequency determination in GIS environments—new software tool for ArcGIS. Planet. Space Sci. 59, 1243–1254. https://doi.org/10.1016/j.pss.2010.03.015.

Kress, A.M., Head, J.W., 2015. Late Noachian and early Hesperian ridge systems in the south circumpolar Dorsa Argentea Formation, Mars: evidence for two stages of melting of an extensive late Noachian ice sheet. Planet. Space Sci. 109–110, 1–20. https://doi.org/10.1016/j.pss.2014.11.025.

Krüger, J., Kjær, K.H., 2000. De-icing progression of ice-cored moraines in a humid, subpolar climate, Kötlujökull, Iceland. The Holocene 10, 737–747. https://doi.org/10.1191/095968300094980.

Lefort, A., Burr, D.M., Beyer, R.A., Howard, A.D., 2012. Inverted fluvial features in the Aeolis-Zephyria Plana, western Medusae Fossae Formation, Mars: evidence for post-formation modification. J. Geophys. Res. Planets 117, E03007. https://doi.org/10.1029/2011JE004008.

Maizels, J.K., 1987. Plio-Pleistocene raised channel systems of the western Sharqiya (Wahiba), Oman. Geol. Soc. Lond., Spec. Publ. 35, 31–50. https://doi.org/10.1144/GSL.SP.1987.035.01.04.

Malin, M.C., Bell, J.F., Cantor, B.A., Caplinger, M.A., Calvin, W.M., Clancy, R.T., Edgett, K.S., Edwards, L., Haberle, R.M., James, P.B., Lee, S.W., Ravine, M.A., Thomas, P.C., Wolff, M.J., 2007. Context Camera Investigation on board the Mars Reconnaissance Orbiter. J. Geophys. Res. 112, E05S04 https://doi.org/10.1029/2006JE002808.

Mangold, N., Adeli, S., Conway, S., Ansan, V., Langlais, B., 2012. A chronology of early Mars climatic evolution from impact crater degradation. J. Geophys. Res. Planets 117. https://doi.org/10.1029/2011JE004005.

Masursky, H., Boyce, J.M., Dial, A.L., Schaber, G.G., Strobell, M.E., 1977. Classification and time of formation of Martian channels based on Viking data. J. Geophys. Res. 82, 4016–4038. https://doi.org/10.1029/JS082i028p04016.

Mayer, D.P., Kite, E.S., 2016. An Integrated Workflow for Producing Digital Terrain Models of Mars from CTX and HiRISE Stereo Data Using the NASA Ames Stereo Pipeline. Lunar and Planetary Science Conference XLVII Abstract #1241.

McEwen, A.S., Eliason, E.M., Bergstrom, J.W., Bridges, N.T., Hansen, C.J., Delamere, W. A., Grant, J.A., Gulick, V.C., Herkenhoff, K.E., Keszthelyi, L., Kirk, R.L., Mellon, M.T., Squyres, S.W., Thomas, N., Weitz, C.M., 2007. Mars Reconnaissance Orbiter's High Resolution Imaging Science Experiment (HiRISE). J. Geophys. Res. 112, E05S02 https://doi.org/10.1029/2005JE002605.

Metzger, S.M., 1992. The Eskers of New York State: Formation Process Implications and Esker-Like Features on the Planet Mars. Lunar and Planetary Science Conference XXIII. Abstract #1448.

Michael, G.G., Platz, T., Kneissl, T., Schmedemann, N., 2012. Planetary surface dating from crater size–frequency distribution measurements: spatial randomness and clustering. Icarus 218, 169–177. https://doi.org/10.1016/j.icarus.2011.11.033.

Neukum, G., Jaumann, R., The HRSC Co-Investigator and Experiment Team, 2004. HRSC: the high resolution stereo camera of Mars Express. In: Wilson, A. (Ed.), Mars Express: The Scientific Payload, European Space Agency Special Publication, 1240, pp. 17–35.

Orosei, R., Lauro, S.E., Pettinelli, E., Cicchetti, A., Coradini, M., Cosciotti, B., Paolo, F.D., Flamini, E., Mattei, E., Pajola, M., Soldovieri, F., Cartacci, M., Cassenti, F., Frigeri, A., Giuppi, S., Martufi, R., Masdea, A., Mitri, G., Nenna, C., Noschese, R., Restano, M., Seu, R., 2018. Radar evidence of subglacial liquid water on Mars. Science. https://doi.org/10.1126/science.aar7268 eaar7268.

Pain, C.F., Oilier, C.D., 1995. Inversion of relief — a component of landscape evolution. Geomorphology 12, 151–165. https://doi.org/10.1016/0169-555X(94)00084-5.

Pain, C.F., Clarke, J.D.A., Thomas, M., 2007. Inversion of relief on Mars. Icarus 190 (Part 2), 478–491. https://doi.org/10.1016/j.icarus.2007.03.017.

Peel, S.E., Fassett, C.I., 2013. Valleys in pit craters on Mars: characteristics, distribution, and formation mechanisms. Icarus 225, 272–282. https://doi.org/10.1016/j.icarus.2013.03.031.

Perkins, A.J., Brennand, T.A., Burke, M.J., 2016. Towards a morphogenetic classification of eskers: implications for modelling ice sheet hydrology. Quat. Sci. Rev. 134, 19–38. https://doi.org/10.1016/j.quascirev.2015.12.015.

Petersen, E.I., Holt, J.W., Levy, J.S., 2018. High ice purity of Martian lobate debris aprons at the regional scale: evidence from an orbital radar sounding survey in

Deuteronilus and Protonilus Mensae. Geophys. Res. Lett. 45, 11,595–11,604.
https://doi.org/10.1029/2018GL079759.

Plaut, J.J., Safaeinili, A., Holt, J.W., Phillips, R.J., Head, J.W., Seu, R., Putzig, N.E., Frigeri, A., 2009. Radar evidence for ice in lobate debris aprons in the mid-northern latitudes of Mars. Geophys. Res. Lett. 36, L02203 https://doi.org/10.1029/2008GL036379.

Robbins, S.J., Hynek, B.M., 2012. A new global database of Mars impact craters ≥1 km: 2. Global crater properties and regional variations of the simple-to-complex transition diameter. J. Geophys. Res. 117, E06001 https://doi.org/10.1029/2011JE003967.

Schumm, S.A., 1963. Sinuosity of Alluvial Rivers on the Great Plains. GSA Bull. 74, 1089–1100. https://doi.org/10.1130/0016-7606(1963)74[1089,SOAROT]2.0.CO;2.

Shreve, R.L., 1972. Movement of water in glaciers. J. Glaciol. 11, 205–214. https://doi.org/10.3189/S002214300002219X.

Shreve, R.L., 1985. Esker characteristics in terms of glacier physics, Katahdin esker system, Maine. Geol. Soc. Am. Bull. 96, 639–646. https://doi.org/10.1130/0016-7606(1985)96<639:ECITOG>2.0.CO;2.

Smith, D.E., Zuber, M.T., Frey, H.V., Garvin, J.B., Head, J.W., Muhleman, D.O., Pettengill, G.H., Phillips, R.J., Solomon, S.C., Zwally, H.J., Banerdt, W.B., Duxbury, T.C., Golombek, M.P., Lemoine, F.G., Neumann, G.A., Rowlands, D.D., Aharonson, O., Ford, P.G., Ivanov, A.B., Johnson, C.L., McGovern, P.J., Abshire, J.B., Afzal, R.S., Sun, X., 2001. Mars Orbiter Laser Altimeter: experiment summary after the first year of global mapping of Mars. J. Geophys. Res. 106, 23689–23722. https://doi.org/10.1029/2000JE001364.

Sori, M., Bramson, A.M., 2019. Water on Mars, with a grain of salt: local heat anomalies are required for basal melting of ice at the south pole today. Geophys. Res. Lett. 46, 1222–1231.

Squyres, S.W., 1979. The distribution of lobate debris aprons and similar flows on Mars. J. Geophys. Res. 84, 8087–8096. https://doi.org/10.1029/JB084iB14p08087.

Storrar, R.D., Stokes, C.R., Evans, D.J.A., 2014. Morphometry and pattern of a large sample (>20,000) of Canadian eskers and implications for subglacial drainage beneath ice sheets. Quat. Sci. Rev. 105, 1–25. https://doi.org/10.1016/j.quascirev.2014.09.013.

Tanaka, K.L., Kolb, E.J., 2001. Geologic history of the polar regions of Mars based on Mars global surveyor data I. Noachian and Hesperian Periods. Icarus 154, 3–21. https://doi.org/10.1006/icar.2001.6675.

Tanaka, K.L., Skinner, J.A., Dohm, J.M., Irwin III, R.P., Kolb, E.J., Fortezzo, C.M., Platz, T., Michael, G.G., Hare, T., 2014a. Geologic Map of Mars, US Geologic Survey Scientific Investigations Map 3292, scale 1:20,000,000, with 43 p. pamphlet.

Tanaka, K.L., Skinner, J.A., Dohm, J.M., Irwin III, R.P., Kolb, E.J., Fortezzo, C.M., Platz, T., Michael, G.G., Hare, T., 2014b. Geologic Map of Mars, Pamphlet to accompany Scientific Investigations Map 3292. US Geological Survey.

Vijayan, S., Sinha, R.K., Harish, Anilkumar, R., 2020. Evidence for multiple superposed fluvial deposits within Reuyl Crater, Mars. J. Geophys. Res. Planets 125. https://doi.org/10.1029/2019JE006136 e2019JE006136.

Warner, N.H., Gupta, S., Calef, F., Grindrod, P., Boll, N., Goddard, K., 2015. Minimum effective area for high resolution crater counting of martian terrains. Icarus 245, 198–240. https://doi.org/10.1016/j.icarus.2014.09.024.

Williams, R.M.E., Chidsey Jr., T.C., Eby, D.E., 2007. Exhumed paleochannels in central Utah—Analogs for raised curvilinear features on Mars. In: Hylland, M.D., Clark, D.L., Chidsey, T.C. (Eds.), Central Utah – Diverse Geology of a Dynamic Landscape. Utah Geological Association Publication.

Williams, R.M.E., Irwin, R.P., Burr, D.M., Harrison, T., McClelland, P., 2013. Variability in martian sinuous ridge form: Case study of Aeolis Serpens in the Aeolis Dorsa, Mars, and insight from the Mirackina paleoriver, South Australia. Icarus 225, 308–324. https://doi.org/10.1016/j.icarus.2013.03.016.